



HERUS: A CO ATLAS FROM SPIRE SPECTROSCOPY OF LOCAL ULIRGS

CHRIS PEARSON^{1,2,3}, DIMITRA RIGOPOULOU^{1,3}, PETER HURLEY⁴, DUNCAN FARRAH⁵, JOSE AFONSO^{6,7}, JERONIMO BERNARD-SALAS⁸, COLIN BORYS⁹, DAVID L. CLEMENTS¹⁰, DIANE CORMIER¹¹, ANDREAS EFSTATHIOU¹², EDUARDO GONZALEZ-ALFONSO¹³,

VIANNEY LEBOUTEILLER^{14,15}, AND HENRIK SPOON¹⁵

¹ RAL Space, CCLRC Rutherford Appleton Laboratory, Chilton, Didcot, Oxfordshire OX11 0QX, UK

² Department of Physical Sciences, The Open University, Milton Keynes, MK7 6AA, UK

³ Oxford Astrophysics, Denys Wilkinson Building, University of Oxford, Keble Rd, Oxford OX1 3RH, UK

⁴ Department of Physics and Astronomy, University of Sussex, Falmer, Brighton BN1 9QH, UK

⁵ Department of Physics, Virginia Tech, Blacksburg, VA 24061, USA

⁶ Instituto de Astrofísica e Ciências do Espaço, Universidade de Lisboa, OAL, Tapada da Ajuda, PT1349-018 Lisboa, Portugal

⁷ Departamento de Física, Faculdade de Ciências, Universidade de Lisboa, Edifício C8, Campo Grande, PT1749-016 Lisbon, Portugal

⁸ The Open University, MK7 6, AA Milton Keynes, UK

⁹ Riot Games, 12333 W Olympic Blvd, Los Angeles, CA 90064, USA

¹⁰ Astrophysics Group, Imperial College London, Blackett Laboratory, Prince Consort Rd, London SW7 2AZ, UK

¹¹ Institut für theoretische Astrophysik, Zentrum für Astronomie der Universität Heidelberg, Albert-Ueberle Str. 2, D-69120 Heidelberg, Germany

¹² School of Sciences, European University Cyprus, Diogenes Street, Engomi, 1516 Nicosia, Cyprus

¹³ Universidad de Alcalá de Henares, Departamento de Física, Campus Universitario, E-28871 Alcalá de Henares, Madrid, Spain

¹⁴ CEA-Saclay, DSM/IRFU/SAP, F-91191 Gif-sur-Yvette, France

¹⁵ Cornell University, CRSR, Space Sciences Building, Ithaca, NY 14853, USA

Received 2016 April 18; revised 2016 August 19; accepted 2016 September 9; published 2016 November 14

ABSTRACT

We present the *Herschel* SPIRE Fourier Transform Spectroscopy (FTS) atlas for a complete flux-limited sample of local ultraluminous infrared galaxies (ULIRGs) as part of the HERschel Ultra Luminous InfraRed Galaxy Survey (HERUS). The data reduction is described in detail and was optimized for faint FTS sources, with particular care being taken for the subtraction of the background, which dominates the continuum shape of the spectra. To improve the final spectra, special treatment in the data reduction has been given to any observation suffering from artifacts in the data caused by anomalous instrumental effects. Complete spectra are shown covering 200–671 μm, with photometry in the SPIRE bands at 250, 350, and 500 μm. The spectra include near complete CO ladders for over half of our sample, as well as fine structure lines from [C I] 370 μm, [C I] 609 μm, and [N II] 205 μm. We also detect H₂O lines in several objects. We construct CO spectral line energy distributions (SLEDs) for the sample, and compare their slopes with the far-infrared (FIR) colors and luminosities. We show that the CO SLEDs of ULIRGs can be broadly grouped into three classes based on their excitation. We find that the mid-*J* ($5 < J < 8$) lines are better correlated with the total FIR luminosity, suggesting that the warm gas component is closely linked to recent star formation. The higher *J* transitions do not linearly correlate with the FIR luminosity, consistent with them originating in hotter, denser gas that is unconnected to the current star formation. We conclude that in most cases more than one temperature component is required to model the CO SLEDs.

Key words: infrared: galaxies – galaxies: evolution – galaxies: star formation

1. INTRODUCTION

Among the most luminous objects in the low-redshift ($z \leq 0.2$) universe are the ultraluminous infrared galaxies (ULIRGs, $L(8\text{--}1000)\mu\text{m} > 10^{12}L_\odot$, Soifer et al. 1986; Sanders et al. 1988; Lonsdale et al. 2006), with star formation rates of up to several hundred $M_\odot\text{ yr}^{-1}$. Although low-redshift ULIRGs are rare, with a space density similar to QSOs (0.001 per deg⁻²), their contribution to the co-moving star formation rate density increases dramatically with redshift, by approximately three orders of magnitude by $z = 1$ (Clements et al. 1996; Kim & Sanders 1998; Le Floc'h et al. 2005; Murphy et al. 2011), making them an important population for understanding the cosmic history of stellar and supermassive black hole assembly.

Recent studies, especially from ESA's *Herschel Space Observatory* (Pilbratt et al. 2010), have shown that the low-redshift ULIRGs may not be direct analogs of their high-redshift counterparts. In the local universe, ULIRGs are invariably mergers hosting compact (<kpc) star-forming regions and active galactic nuclei (AGNs; e.g., Melnick & Mirabel 1990; Clements et al. 1996; Rigopoulou et al. 1999;

Soifer et al. 2000; Farrah et al. 2001), but at higher redshifts ULIRGs may host more extended star-forming regions, and may be associated both with interacting and isolated galaxies (e.g., Pope et al. 2006; Farrah et al. 2008; Magdis et al. 2011; Symeonidis et al. 2013; Béthermin et al. 2014). The high-redshift ULIRGs thus lie on the galaxy mass-specific star formation rate density relation (the so-called “main sequence”), making them typical rather than extreme at these redshifts (e.g., Elbaz et al. 2011).

An invaluable tool for understanding why this change in the properties and importance of ULIRGs with redshift occurs is infrared spectroscopy, since it probes the ionization conditions of the interstellar medium and star-forming regions. In particular, infrared spectroscopy can probe the large reservoirs of carbon monoxide (CO) in ULIRGs, which trace the total molecular gas reservoir, by constructing their CO spectral line energy distributions (SLEDs; Sanders et al. 1991; Downes et al. 1993; Wolfire et al. 2010). The lower rotational transitions, CO(1–0) up to about CO(3–2), trace the total cold dense gas (e.g., Sanders et al. 1991; Solomon et al. 1997), while the higher *J* transitions trace the warmer gas associated

with the PDR and XDR regions. Therefore, to trace the different temperature components within the gas, observations covering many CO transitions are required. However, since only the low- J lines ($J < 6$) are accessible from the ground, observations with *Herschel* over the CO(5–4) up to CO(13–12) range are necessary to discriminate the contributions from UV and X-ray excitation via star formation and AGNs, respectively (e.g., Meijerink & Spaans 2005). Observations of the CO SLED in low-redshift ULIRGs can also be used as templates for comparison for intermediate to high redshift (e.g., Greve et al. 2014). In addition, far-infrared (FIR) spectroscopy allows access to several important fine structure lines, which provide complementary diagnostics of ISM conditions. For example, low-redshift ULIRGs show a deficit in the strength of their [C II] fine structure line at 158 μm relative to the FIR dust continuum compared to lower luminosity galaxies (e.g., Luhman et al. 1998, 2003; Farrah et al. 2013), but this deficit is not apparent at higher redshift (Hailey-Dunsheath et al. 2010b; Stacey et al. 2010; Magdis et al. 2014).

In this paper, we report on a comprehensive *Herschel* survey of a flux-limited sample of low-redshift ULIRGs, producing a CO atlas that includes all ULIRGs in the universe out to $z = 0.2$. An extensive CO spectral atlas of extragalactic objects has also been published in Kamenetsky et al. (2016). In Section 2, we introduce the source sample and describe the *Herschel* observations. In Section 3 we describe the data reduction steps using standard processing pipelines and also the post-processing steps required to produce the final spectra. In Section 4, we describe our line-fitting procedure, providing identifications and line fluxes for our sample. Our results are presented in Section 5. A discussion and our conclusions are given in Sections 6 and 7. A detailed analysis of the CO SLED fits will be presented in P.D. Hurley et al. (2016, in preparation). We assume a Hubble constant of $H_0 = 70 \text{ km s}^{-1} \text{ Mpc}^{-1}$ and density parameters of $\Omega_M = 0.3$ and $\Omega_\Lambda = 0.7$.

2. OBSERVATIONS

The HERschel Ultra Luminous InfraRed Galaxy Survey (HERUS, PI Farrah) was the largest extragalactic Open Time survey (OT1, 250 hr) carried out by the *Herschel Space Observatory*. HERUS is a flux-limited sample of low-redshift ULIRGs comprising the 43 ULIRGs from the *IRAS* PSC-z survey (Saunders et al. 2000) with 60 μm fluxes greater than 1.8 Jy (Table 1).

The sample was observed by *Herschel* using the Spectral and Photometric Imaging REceiver (SPIRE, Griffin et al. 2010) in both photometry (250, 350, 500 μm) and spectroscopy using the SPIRE Fourier Transform Spectrometer, (FTS; Swinyard et al. 2010) from 194 to 671 μm (except 3C273, which only has photometric data). The SPIRE photometry and spectroscopy observations were carried out between 2011 July 26th (*Herschel* Operational Day, OD804) and 2012 October 19th (OD 1178). The observations are summarized in Table 1. The SPIRE photometer observations were carried out in Small Map mode (*SpirePhotoSmallScan*, POF1;, Dowell et al. 2010) with fixed, three-repetition (445 s), cross-linked 1 \times 1 scan legs covering a field of 4' radius. Images are taken simultaneously in the SPIRE 250 μm (PSW), 350 μm (PMW), and 500 μm (PLW) bands. Note that 3C273 only has photometric data and the photometric data for IRAS 06035-7102 were in fact extracted from the Open

Time Key Programme: KPOT_mmeixner observations of the Large Magellanic Cloud, Level 2.5 *Herschel* data product.

SPIRE spectroscopic observations were made in Point Source Spectroscopy mode (*SpireSpectroPoint*, SOF1; Fulton et al. 2010) with high spectral resolution (HR; 0.048 cm^{-1}), and sparse spatial sampling. Observations ranged from 45 to 100 repetitions (forward + reverse scans of the FTS, 6316 s—13752 s) depending on the predicted source continuum level. The SPIRE FTS measures the Fourier transform of the spectrum of a source with two bolometer detector arrays (see Figure 1); the Spectrometer Short Wavelength (SSW) and Spectrometer Long Wavelength (SLW) simultaneously covering the entire wavelength range from 194 to 313 μm (SSW) and 303–671 μm (SLW), respectively. Although the spectrometer arrays have 37 detectors (SSW) and 19 detectors (SLW), only the central SSW D4 and SLW C3 detectors are used for the point source spectrum. In addition to the target spectroscopic observations, the corresponding instrument *Dark Sky obsid* intended for background subtraction, for each spectroscopic observation, is also listed (Section 3). These dark skies were supplied by the SPIRE Instrument Control Centre (ICC) on an observational day basis and were not attached specifically to the observation program itself. Observations that were included in our data processing from *Herschel* archival data but were not within the HERUS program itself are denoted by asterisks. The spectroscopic observation of IRAS 07598+6508 had to be repeated due to a pointing error in the initial observation (obsid = 1342231979), but the photometric data were still usable.

FIR spectroscopy was made using the *Herschel* Photodetector Array Camera and Spectrometer (PACS; Poglitsch et al. 2010). Observations with PACS for the 43 ULIRGs were split between the HERUS program (Farrah et al. 2013; Spoon et al. 2013) and the SHINING program (Fischer et al. 2010; Sturm et al. 2011; Hailey-Dunsheath et al. 2012a; González-Alfonso et al. 2013; Mashian et al. 2015). A similar study of the intermediate redshift ULIRG population ($0.21 < z < 0.88$) was presented by Rigopoulou et al. (2014) and Magdis et al. (2014). The entire sample has already been observed (Armus et al. 2007; Farrah et al. 2007) with the Infrared Spectrograph (IRS, Houck et al. 2004) on board *Spitzer* (Werner et al. 2004).

3. DATA REDUCTION

3.1. Pipeline

All spectrometer data were processed through the Spectrometer Single Pointing User Pipeline (Fulton et al. 2010, 2016) within the *Herschel* Common Science System *Herschel Interactive Processing Environment* (HIPE Ott et al. 2010). All the data were reprocessed with HIPE v11.2757 SPIRE Calibration Tree version 11.0. HIPE v11 generally improves the sensitivity levels predicted by HSpot¹⁶ over the entire FTS wavelength range, by ~ 0.05 Jy for a 1 hr observation (i.e., approximately 20% improvement). The error on the continuum shape also improves, with an average reduction in the offset of 0.08 Jy. This is due to the higher signal-to-noise in the flux calibration and is particularly important for the relatively faint lines in many of the HERUS sample (The improvements are most significant for observations taken after OD 998). Full details of the treatment of faint sources with the SPIRE FTS

¹⁶ *Herschel* Observation Planning Tool.

Table 1
Summary of HERUS Observations of Local ULIRGs

Name	Redshift	$\log(L_{\text{IR}})$ L_{\odot}	Photometer		Spectrometer		
			OD	ObsID	OD	ObsID	Dark ObsID
IRAS 00397-1312	0.262	12.97	949	1342234696	1111	1342246257	1342246261
Mrk 1014	0.163	12.61	976	1342237540	998	1342238707 ^a	1342238702
3C273	0.158	12.72	948	1342234882
IRAS 03521+0028	0.152	12.56	1022	1342239850	997	1342238704	1342231982
IRAS 07598+6508	0.148	12.46	862	1342229642	1255	1342253659	1342253653
IRAS 10378+1109	0.136	12.38	948	1342234867	1131	1342247118	1342247109
IRAS 03158+4227	0.134	12.6	825	1342226656	804	1342224764	1342224758
IRAS 16090-0139	0.134	12.54	862	1342229565	997	1342238699	1342238702
IRAS 20100-4156	0.13	12.63	880	1342230817	1079	1342245106	1342245125
IRAS 23253-5415	0.13	12.4	949	1342234737	1112	1342246277	1342246261
IRAS 00188-0856	0.128	12.47	949	1342234693	1111	1342246259	1342246261
IRAS 12071-0444	0.128	12.4	948	1342234858	1161	1342248239	1342248235
IRAS 13451+1232	0.122	12.32	948	1342234792 ^a	972	1342237024 ^a	1342236999
IRAS 01003-2238	0.118	12.3	949	1342234707	1111	1342246256	1342246261
IRAS 11095-0238	0.107	12.28	948	1342234863	1151	1342247760	1342247753
IRAS 20087-0308	0.106	12.41	880	1342230838	885	1342231049	1342231052
IRAS 23230-6926	0.106	12.32	880	1342230806	1112	1342246276	1342246261
IRAS 08311-2459	0.1	12.46	880	1342230796	879	1342230421	1342230416
IRAS 15462-0450	0.099	12.24	989	1342238307	1178	1342249045	1342249068
IRAS 06206-6315	0.092	12.23	825	1342226638	885	1342231038	1342231052
IRAS 20414-1651	0.087	12.24	892	1342231345	1054	1342243623	1342243620
IRAS 19297-0406	0.086	12.38	880	1342230837	886	1342231078	1342231052
IRAS 14348-1447	0.083	12.33	989	1342238301	1186	1342249457	1342249454
IRAS 06035-7102	0.079	12.2	353	1342195728 ^a	879	1342230420	1342230416
IRAS 22491-1808	0.078	12.18	949	1342234671	1080	1342245082	1342245125
IRAS 14378-3651	0.067	12.14	989	1342238295	824	1342227456	1342227459
IRAS 23365+3604	0.064	12.17	948	1342234919	804	1342224768	1342224758
IRAS 19254-7245	0.062	12.06	515	1342206210 ^a	885	1342231039	1342231052
IRAS 09022-3615	0.06	12.24	880	1342230799	886	1342231063 ^a	1342231052
IRAS 08572+3915	0.058	12.1	880	1342230749	907	1342231978	1342231982
IRAS 15250+3609	0.055	12.03	948	1342234775	998	1342238711	1342238702
Mrk 463	0.05	11.77	963	1342236151	1178	1342249047	1342249068
IRAS 23128-5919	0.045	12	544	1342209299 ^a	1079	1342245110 ^a	1342245125
IRAS 05189-2524	0.043	12.12	467	1342203632 ^a	317	1342192833 ^a	1342192838
IRAS 10565+2448	0.043	12	948	1342234869	1130	1342247096	1342247109
IRAS 17208-0014	0.043	12.38	467	1342203587 ^a	317	1342192829 ^a	1342192838
IRAS 20551-4250	0.043	12.01	880	1342230815	1079	1342245107 ^a	1342245125
Mrk 231	0.042	12.49	209	1342201218 ^a	209	1342187893 ^a	1342187890
UGC 5101	0.039	11.95	495	1342204962 ^a	544	1342209278 ^a	1342208391
Mrk 273	0.038	12.13	438	1342201217 ^a	557	1342209850 ^a	1342209858
IRAS 13120-5453	0.031	12.22	829	1342226970	602	1342212342 ^a	1342212320
NGC 6240	0.024	11.8	467	1342203586 ^a	654	1342214831 ^a	1342214832
Arp 220	0.018	12.14	229	1342188687 ^a	275	1342190674 ^a	1342190675

Note. The operational day (OD) and observation identification (obsID) are tabulated for the observations made with the SPIRE photometer and spectrometer. The obsID for the associated spectrometer dark sky is also listed. Indicative far-infrared luminosities ($L_{\text{IR}} = L_{8-1000 \mu\text{m}}$) calculated following Sanders & Mirabel (1996) are included for reference. Note that 3C273 has photometer data but no corresponding spectroscopic data were taken.

^a *Herschel* archival data.

pipeline are explained in Hopwood et al. (2015). In Figure 2, the evolution in data quality as a function of pipeline version is shown for the example of Mrk 231 (obsid = 1342187893). By HIPE v10 the discontinuity between the SPIRE FTS SSW and SLW bands was improved, while the overall noise in the spectrum was further decreased between HIPE v10 and HIPE v11. Figure 2 also shows the typical resulting spectrum from earlier versions (e.g., HIPE v6) of the spectrometer pipeline (e.g., Mrk 231: González-Alfonso et al. 2010; van der Werf et al. 2010, Arp 220: Rangwala et al. 2011, NGC 6240: Meijerink et al. 2013). All the data, both HERUS and archival

in Table 1, have been re-reduced with the HIPE v11 pipeline, using the default values for all pipeline tasks. The pipeline produces *Level 1* products for all the array detectors in the form of extended emission calibrated spectra in $\text{W m}^{-2} \text{Hz}^{-1} \text{sr}^{-1}$ and the final *Level 2* data products as point-source-calibrated unapodized spectra for the central detectors SLW C3 and SSW D4 measured in Jy as a function of frequency in GHz.

Although the current version of the SPIRE spectrometer pipeline is HIPE 14, there has not been a significant improvement in the sensitivity for faint point source spectroscopy since HIPE version 11. The most significant changes in

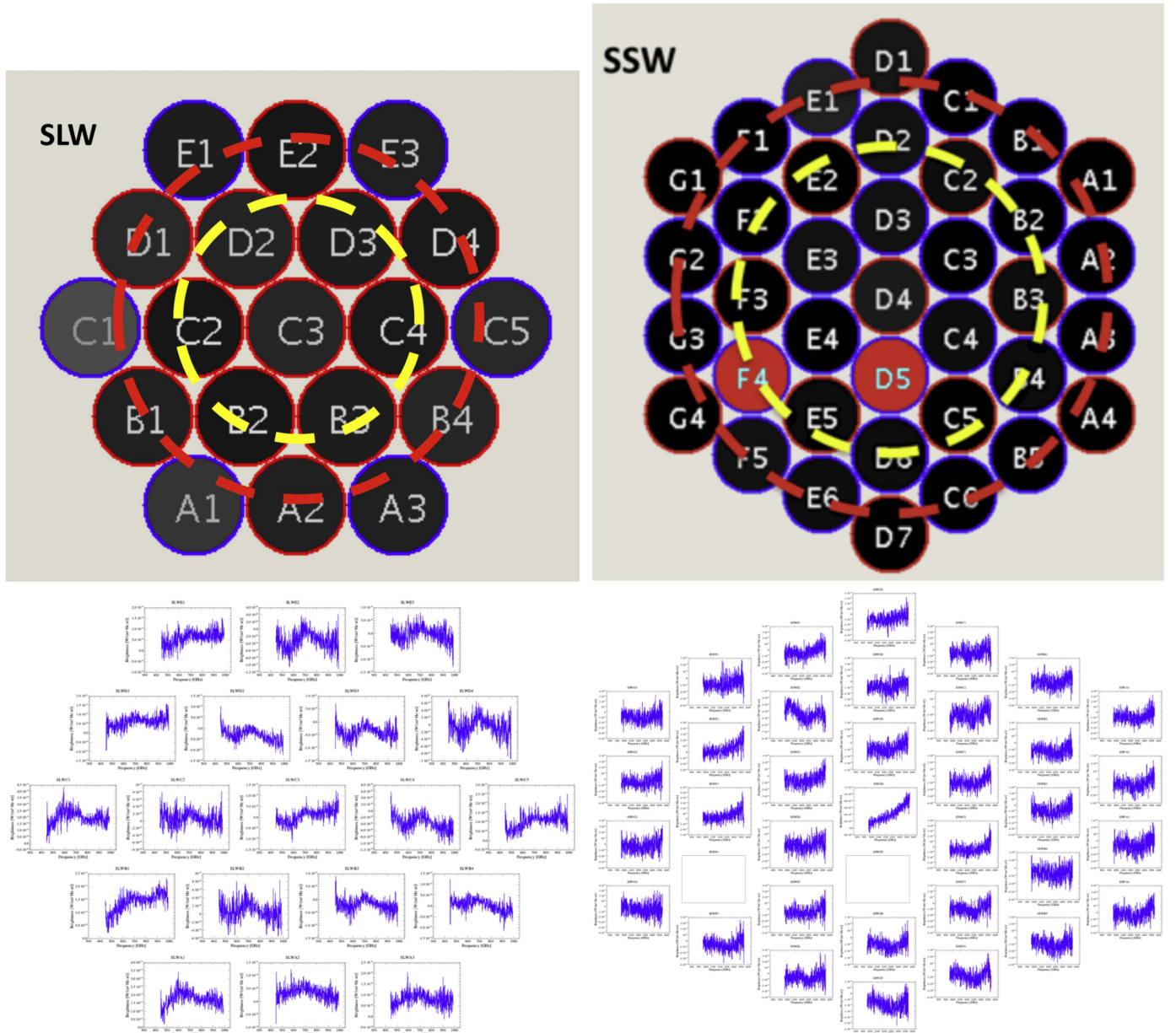


Figure 1. Top: array footprints for the SSW and SLW FTS arrays showing the central SSW D4 and SLW C3 detectors, the inner ring of detectors used for the off-axis background subtraction, and the outer ring of vignetted detectors. Bottom: detector readouts for the observation of IRAS 03158+4227 on OD804 (obsID = 1342224764).

HIPE 14 regard bright sources, extended mapping, and low resolution spectroscopy (Hopwood et al. 2015; Fulton et al. 2016). It should be noted that much of the additional post-pipeline processing described in Section 3.2 has since been incorporated into the standard HIPE 14 pipeline and therefore the results presented in the work would not significantly improve with re-processing using HIPE 14.

Exceptions to the standard pipeline processing were FTS observations made within 8 hr of the beginning of an SPIRE FTS observation period, which were often found to suffer from a decrease or *drooping* in the SLW band flux. The SPIRE cooler was recycled at the beginning of every pair of SPIRE days and in some cases anomalous *Cooler Burps* (see C.P. Pearson et al. 2016, in preparation) caused an outlying low temperature in the instrument 0.3 K cooler stage causing correspondingly low detector temperatures. There was found to be a correlation

between this temperature change (measured by the instrument *SUBKTEMP* sensor) and flux density. This effect was not corrected by the pipeline non-linearity correction and moreover cannot be corrected using a dark sky subtraction since the dark sky is more likely to have an average *SUBKTEMP* and therefore no *droop*. For affected observations, the flux *droop* was empirically corrected within the pipeline using a linear correlation found between the SLW flux density and the *SUBKTEMP* temperature. This correction is shown in Figure 3 for the example of IRAS 01003-2238 (obsid = 1342246256). Note that different detectors were found to have different sensitivities to this issue, e.g., SLWC3 is found to be very sensitive to variations in *SUBKTEMP*, but SSW D4 showed no clear correlation and therefore was not corrected. Observations that were corrected for the *SUBKTEMP* flux *drooping* were IRAS 00397-1312 (1342246256), IRAS 01003-2238 (1342246256), IRAS 06206-

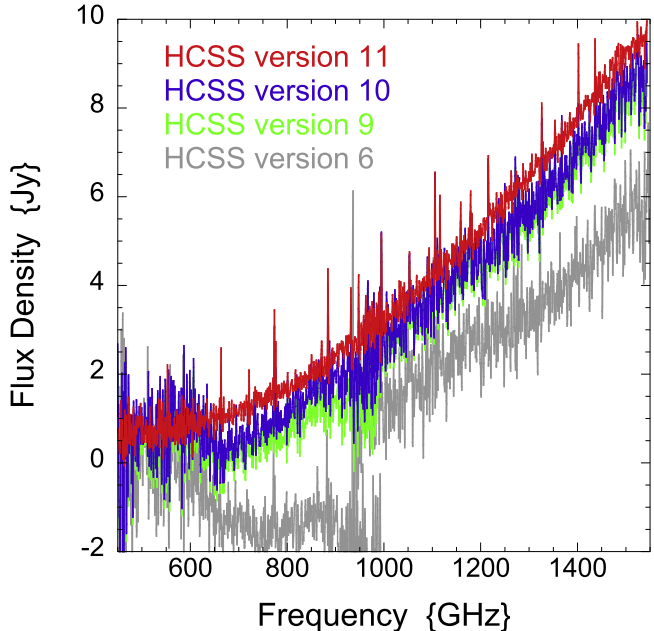


Figure 2. Comparison of the improvement in pipeline processing within the HCSS HIPE environment, for Mrk 231, obsid = 1342187893. The earliest pipeline-processed spectrum shows an offset between the SSW and SLW bands due to sub-optimal subtraction of the telescope emission. The latest HIPE v11 data are processed with either new RSRFs + subtemp correction or new RSRFs + new telescope model correction. The HIPE v11 spectrometer pipeline also features significantly reduced noise compared to HIPE v10.

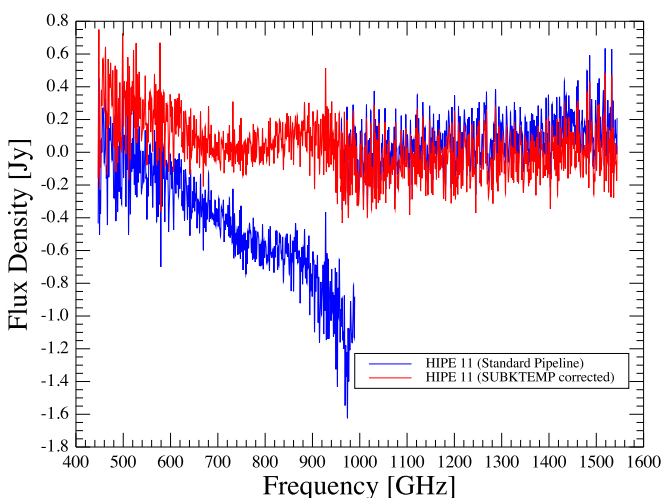


Figure 3. Correction for the flux *drooping* effect exhibit by the SLW C3 central detector for FTS observations taken within 8 hr of a SPIRE cooler recycle with a cooler burp event (obsid = 1342246256). The discontinuity in the standard pipeline-processed observation with HIPE v11 is compared with the corrected continuous spectrum obtained from an empirical correction utilizing the correlation found between the flux density measured by the detector and the *SUBKTEMP* temperature.

6315 (1342231038), IRAS 10565+2448 (1342247096), IRAS 16090-0139 (1342238699), IRAS 20100-4156 (1342245106), IRAS 20551-4250 (1342245107), and IRAS 23128-5919 (1342245110).

Many of the corrections and techniques used in the data reduction in this work have also been incorporated into the standard processing for later versions of HIPE (13.0, 14.0

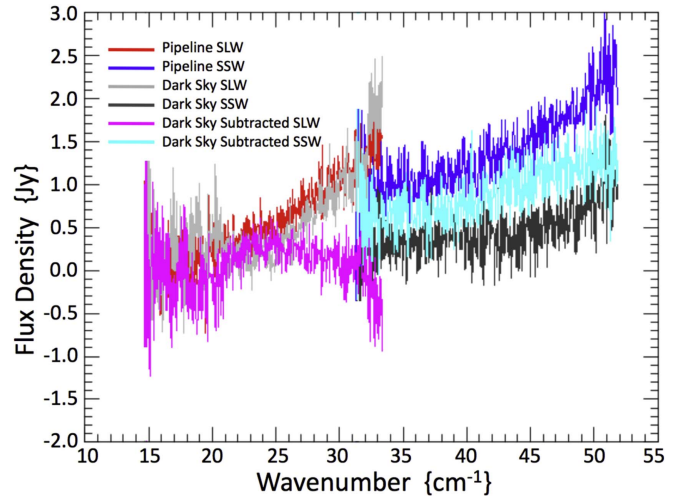


Figure 4. Problems with post-processing background removal using the OD803 dark sky observation associated with the FTS observation of IRAS 03158+4227 (obsid = 1342224764) taken on OD804. Pipeline SLW and Pipeline SSW are the spectra as naively processed by the standard pipeline exhibiting an offset between the two spectral bands. The Dark Sky spectra themselves are labeled *Dark Sky SLW* and *SSW*, respectively. The post-processed, dark-subtracted spectra are shown as *Dark Sky Subtracted SLW* and *SSW*, respectively. Note that the dark sky subtraction method has over-compensated at the short wavelength end of the SLW band.

Hopwood et al. 2015); however, many such cases still need to be processed on a case-by-case basis.

3.2. Post-pipeline Processing

For all but the brightest *Herschel* SPIRE FTS observations, the total measured signal is always dominated by the emission from the \sim 80 K telescope. The contributed flux density corresponding to this emission is of the order of \sim 200–800 Jy. After pipeline processing residual telescope emission causes both a distortion in the overall spectral shape and a discontinuity between the spectra in the SSW and SLW bands, due to the variation of beam size with frequency as shown in the left panel of Figure 4. Swinyard et al. (2014) estimate that the associated offset for the central detectors is \sim 0.4 Jy and \sim 0.29 Jy for SLWC3 and SSW D4, respectively, meaning that the majority of the HERUS sample will be severely affected.

Therefore, in order to correct for discontinuities between the SSW and SLW spectra, post-processing for additional background subtraction is required. Several methods for background subtraction are possible;

1. Use the standard dark sky observation taken on or around the same OD.
2. Use a super-dark averaged from many dark sky observations.
3. Use the off-axis detectors on the spectrometer arrays to produce an effective local dark sky measurement.

For every pair of SPIRE spectrometer days, a generic dark sky observation was taken by the SPIRE ICC with a duration corresponding to the longest FTS observation from any program taken on that pair of ODs. For the HERUS sample the corresponding dark sky observations are listed in Table 1. In Figure 4 the results for the pipeline-processed data for the FTS observation of IRAS 03158+4227 (obsid = 1342224764) taken on OD804 show an offset between the two spectrometer bands

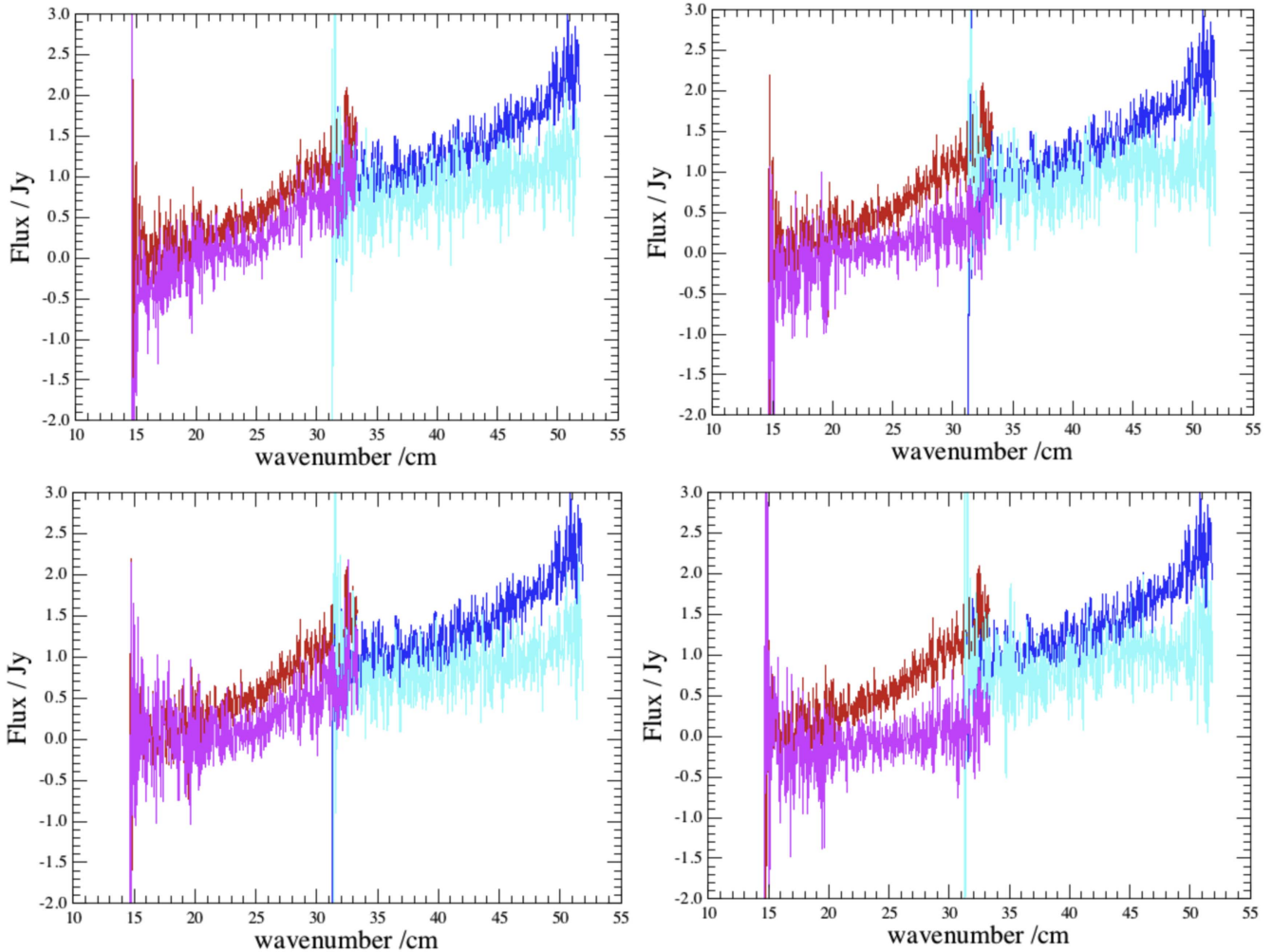


Figure 5. Using the off-axis detectors for the dark subtraction for the observation. The upper lines (red, blue) show the original pipeline spectrum and the lower lines (magenta, cyan) show the spectra after correction by dark subtraction using a specific pair of SSW, SLW off-axis co-aligned detectors that view the same sky as other detectors. From left to right, using SSW C5 and SLW C4 (co-aligned detectors), SSW C5 and SLWB3 (co-aligned detectors), SSW D1 and SLW E2 (co-aligned detectors), SSW D7 and SLW A2 (co-aligned detectors).

SSW, SLW. This offset is due to differences in the background (including telescope) subtraction. In some cases this offset is overcome by subtracting a spectrometer observation of the dark sky with similar integration. In the case of Figure 4, the dark sky observation taken on OD803 (obsID = 1342224758) was used. Unfortunately, the subtraction is unsatisfactory, as sometimes happens when the dark from a different day or different number of repetitions is used (in this case the observation was taken on OD804, while the dark was taken on OD803). Processing using a super-dark averaged from many independent dark sky observations also exhibits similar issues.

An alternative to using the dedicated dark sky or super-dark observations is to use the off-axis (non-central; see Figure 1) detectors to produce an effective local dark observation. The advantage with this option is that the dark observation is effectively taken at the same time as the observation. The disadvantage is that the dark is taken with a different detector to that of the target central detector. A number of detectors on the SSW array are co-aligned (see the same area of sky), so a corresponding detector on the SLW array and these co-aligned detectors were used to evaluate the quality of off-axis detector background subtraction. Figure 5 shows the results of using

different pairs of co-aligned off-axis pairs for the dark subtraction. Unfortunately it was found that the subtraction varies from off-axis detector pair to off-axis detector pair.

In order to overcome the differences from detector to detector, an average background can be computed using the outer rings of non-vignetted detectors on the SSW and SLW arrays, as shown in Figure 1 for the example observation of IRAS 03158+4227 on OD804 (obsID = 1342224764). Note that Figure 1 also shows the footprints of each array with the detector readouts for processed spectra with the target on the central SSW D4 and SLW C3 detectors. It can be seen that there can still be non-negligible outliers within the off-axis detectors. These differences can be due to individual detector performance during an observation or be due to emission from some source or astrophysical background that serendipitously falls on that particular off-axis detector.

Outlier rejection of anomalous off-axis detectors was carried out by inspecting the smoothed spectra from each off-axis detector by eye to reject any outliers, as shown in Figure 6. In addition, the spectrometer array footprint was overlaid on the SPIRE photometer maps to identify cases where the off-axis detectors were adversely affected by any background emission or

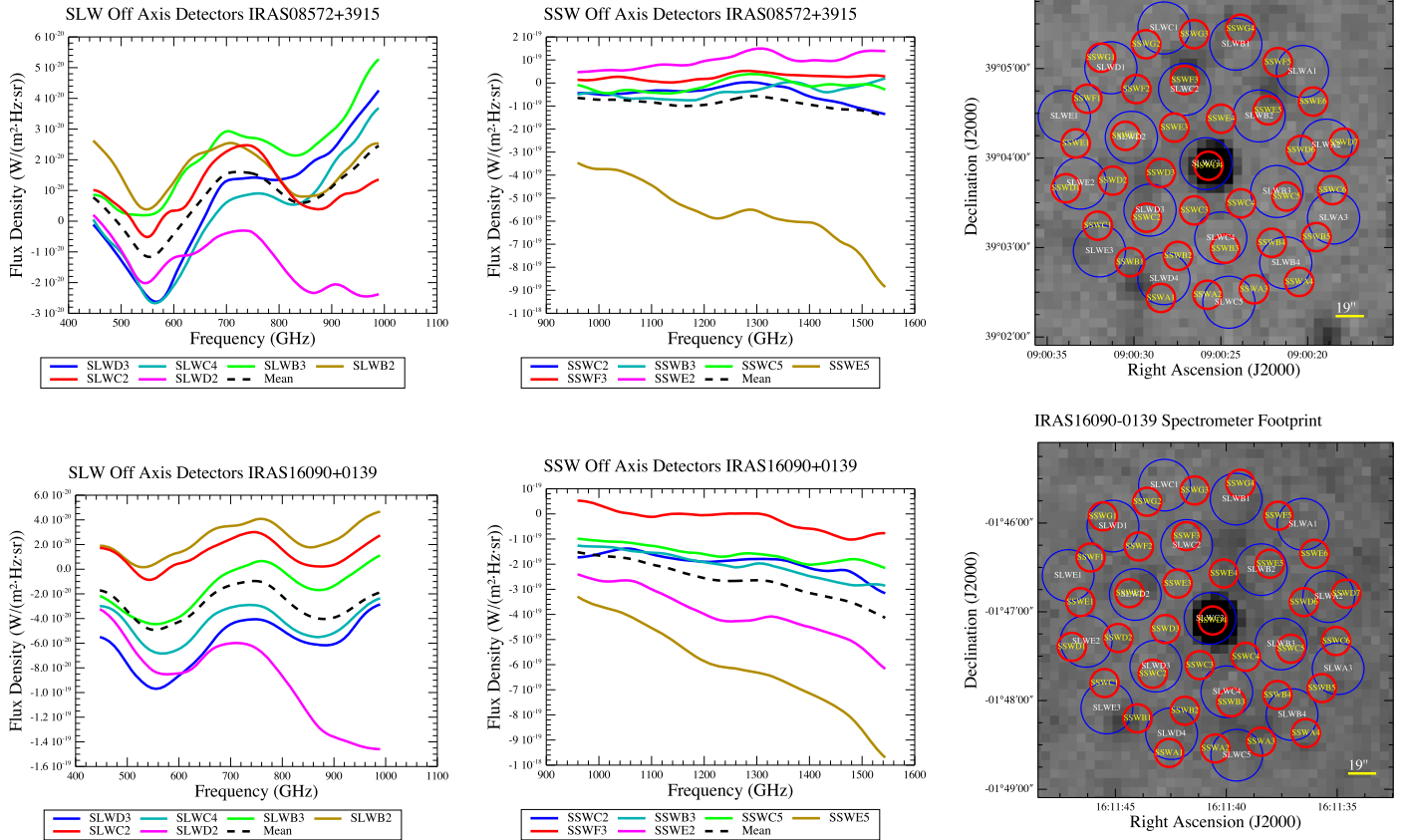


Figure 6. Example of the selection of median-smoothed off-axis detector spectra for background subtraction for the cases of IRAS 08572+3915 and IRAS 16090+0139. Using a combination of the off-axis detector spectra and the inspection of the spectrometer array footprint overlaid on the photometry maps, outliers are rejected and the remaining off-axis detectors are used to form an averaged off-axis super-dark. For IRAS 08572+3915 the SLWD3, SLWB2, and SSWE5 detectors are excluded. For IRAS 16090+0139 the SLWD2, SSWE5, and SSWE2 detectors are excluded. The resulting spectra are shown in Figure 7.

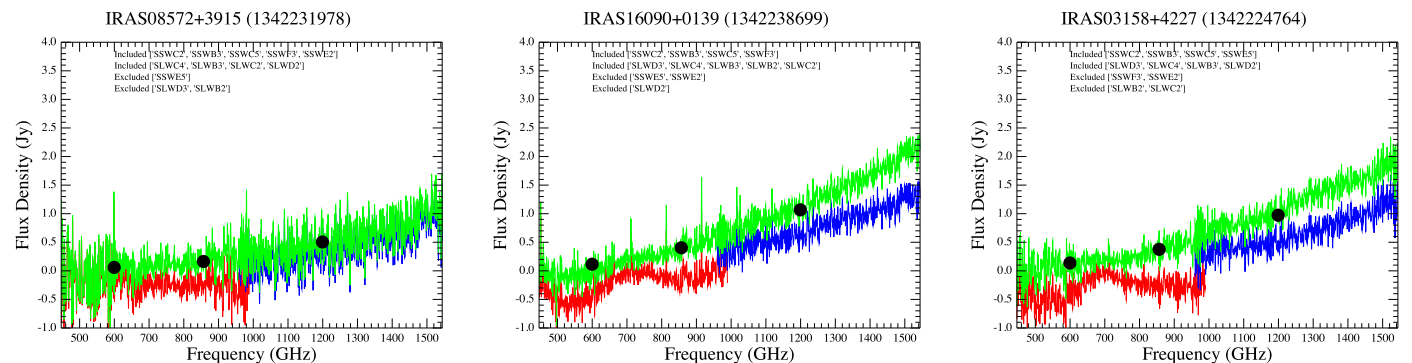


Figure 7. Final spectra (continuous green line) after all post-processing steps described in the text compared with the original pipeline-processed spectra for three HERUS galaxies, IRAS 08572+3915, IRAS 16090+0139, and IRAS 03158+4227 (obsid = 1342231978, 1342238699, and 1342224764, respectively). After the post-processing steps we find that the SSW and SLW band spectra are well-aligned, and that the photometry is in good agreement with the spectra. The SSW and SLW off-axis detectors included and excluded for the dark subtraction are listed. For comparison, the detector spectra before post-processing are shown for the SLW (red) and SSW (blue) arrays.

source serendipitously lying within the detector beam on the sky as shown in the right panels of Figure 6.

The processing steps to obtain the final Level 2 point source calibrated spectra using the off-axis detectors for the background subtraction are as follows.

1. Begin with Level 1 product spectra ($\text{W m}^{-2} \text{ Hz}^{-1} \text{ sr}^{-1}$).
2. Average all (forward and reverse) FTS scans for each individual detector.

3. Inspect the smoothed spectra from the off-axis detectors by eye to reject any outliers as shown in Figure 6.
4. Average all selected off-axis detector spectra to form an off-axis super-dark.
5. Subtract off-axis super-dark from central detector spectra for both the SSW and SLW arrays.
6. Filter Channels (select the central detectors only).

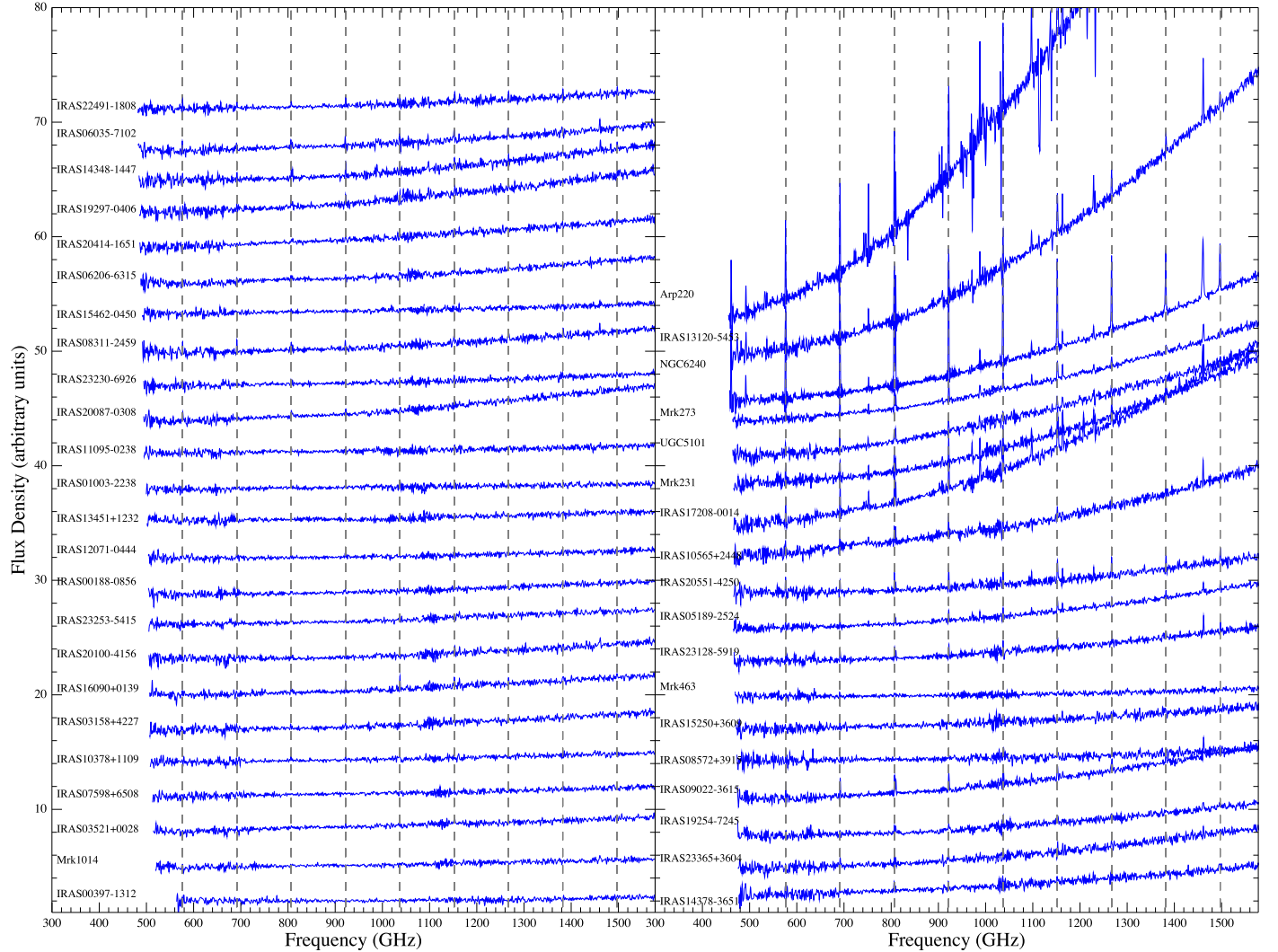


Figure 8. Final processed spectra for all HERUS targets in the rest frame. Targets are ordered from bottom to top and left to right in decreasing redshift. Flux density is in arbitrary offsets for clarity. Also overlaid as dotted lines are the lines on the CO ladder from the CO(5–4), CO(6–5), CO(7–6), CO(8–7), CO(9–8), CO(10–9), CO(11–10), CO(12–11), CO(13–12) transitions at 576, 691, 806, 921, 1036, 1151, 1267, 1381, and 1496 GHz (519, 432, 371, 324, 288, 260, 236, 216, and 200 μm).

7. Carry out the point source calibration on the 2 central detector channels.
8. Final Level 2 point source calibrated spectra (Jy).

Applying this method of off-axis detectors for the dark subtraction results in a much better agreement for the SSW and SLW spectra (e.g., the three representative observations shown in Figure 7, (obsid = 1342231978, 1342238699 and 1342224764). In almost all cases the corrected spectral continuum level agrees well with the measured SPIRE photometry (see Section 3.4) for SSW (250 μm band) and SLW (350 μm , 500 μm bands). In order to remove any residual background, the baseline is subtracted by fitting a three-order polynomial to the continuum and then fitting to the SPIRE photometry points using a polynomial fit for the photometer to normalize the spectrum baseline.

The standard spectrometer pipeline assumes that the source is a point source on the central detector. However, if a source is extended with respect to the beam there may be a discontinuity in the overlapping spectral region between the short and long wavelength bands due to the sudden change in the effective beam size at those frequencies, given that the SLW beam diameter is approximately twice that of the SSW beam

diameter. The discontinuities found for extended sources can be corrected using the dedicated Semi-Extended Correction Tool (SECT) within HIPE. The SECT tool allows for the fitting of a Gaussian model for a source and corrects the spectra continuum and flux accordingly.

We have identified possible extended sources within our sample by comparing the photometer maps with either the Photometer beam or the FTS footprint as shown in Figure 6. A source is flagged as being possibly extended if it falls within the first external ring of FTS detectors. Sources that fall within the category are IRAS 10565+2448, IRAS 13120-5453, IRAS 17208-0014, NGC 6240, and UGC 5101. To correct them, we have followed the procedure detailed in Wu et al. (2013) using the SECT tool within HIPE but find only small differences, of 1% to <5%.

3.3. Final Spectra

After the pipeline processing (including *SUBKTEMP* correction where necessary) and the post-processing, including the background subtraction using the off-axis detectors, fitting to the SPIRE photometry and correction for any extension, the

Table 2
Photometry of the HERUS Galaxies in the SPIRE Bands PSW (250 μm), PMW (350 μm), and PLW (500 μm)

Target	obsid	PSW		PMW		PLW	
		Flux Density Jy^{-1}	Error Jy^{-1}	Flux Density Jy^{-1}	Error Jy^{-1}	Flux Density Jy^{-1}	Error Jy^{-1}
IRAS 00397-1312	1342234696	0.389	0.004	0.130	0.004	0.040	0.005
Mrk 1014	1342237540	0.460	0.004	0.175	0.004	0.063	0.005
3C273	1342234882	0.437	0.004	0.633	0.004	0.994	0.005
IRAS 03521+0028	1342239850	0.684	0.004	0.270	0.004	0.094	0.004
IRAS 07598+6508	1342229642	0.500	0.004	0.197	0.004	0.058	0.005
IRAS 10378+1109	1342234867	0.480	0.004	0.183	0.004	0.050	0.005
IRAS 03158+4227	1342226656	0.973	0.004	0.377	0.004	0.137	0.005
IRAS 16090-0139	1342229565	1.067	0.004	0.404	0.004	0.116	0.005
IRAS 20100-4156	1342230817	1.001	0.004	0.349	0.004	0.102	0.005
IRAS 23253-5415	1342234737	1.044	0.005	0.437	0.004	0.165	0.005
IRAS 00188-0856	1342234693	0.877	0.004	0.345	0.004	0.111	0.005
IRAS 12071-0444	1342234858	0.471	0.004	0.163	0.004	0.044	0.005
IRAS 13451+1232	1342234792	0.503	0.005	0.256	0.004	0.197	0.006
IRAS 01003-2238	1342234707	0.222	0.004	0.070	0.004	0.026	0.006
IRAS 23230-6926	1342230806	0.617	0.004	0.204	0.004	0.064	0.005
IRAS 11095-0238	1342234863	0.380	0.004	0.119	0.004	0.036	0.005
IRAS 20087-0308	1342230838	1.804	0.006	0.687	0.004	0.210	0.005
IRAS 15462-0450	1342238307	0.492	0.004	0.162	0.004	0.050	0.008
IRAS 08311-2459	1342230796	1.246	0.005	0.464	0.004	0.148	0.005
IRAS 06206-6315	1342226638	1.248	0.005	0.477	0.004	0.158	0.005
IRAS 20414-1651	1342231345	1.315	0.005	0.519	0.004	0.168	0.005
IRAS 19297-0406	1342230837	2.039	0.006	0.752	0.004	0.244	0.005
IRAS 14348-1447	1342238301	1.842	0.006	0.666	0.005	0.197	0.006
IRAS 06035-7102	1342195728	1.226	0.022	0.397	0.001	0.130	0.008
IRAS 22491-1808	1342234671	0.862	0.004	0.305	0.004	0.097	0.005
IRAS 14378-3651	1342238295	1.330	0.005	0.478	0.005	0.135	0.006
IRAS 23365+3604	1342234919	1.849	0.006	0.669	0.004	0.210	0.005
IRAS 19254-7245	1342206210	1.545	0.005	0.587	0.004	0.185	0.005
IRAS 09022-3615	1342230799	2.449	0.007	0.823	0.004	0.252	0.005
IRAS 08572+3915	1342230749	0.504	0.004	0.164	0.004	0.060	0.004
IRAS 15250+3609	1342234775	0.966	0.004	0.368	0.004	0.136	0.005
Mrk 463	1342236151	0.344	0.004	0.134	0.004	0.052	0.005
IRAS 23128-5919	1342209299	1.565	0.008	0.556	0.006	0.176	0.007
IRAS 10565+2448	1342234869	3.619	0.011	1.319	0.004	0.407	0.005
IRAS 20551-4250	1342230815	1.629	0.005	0.556	0.004	0.170	0.005
IRAS 05189-2524	1342203632	1.963	0.011	0.717	0.007	0.211	0.009
IRAS 17208-0014	1342203587	7.918	0.037	2.953	0.010	0.954	0.009
Mrk 231	1342201218	5.618	0.019	2.011	0.008	0.615	0.008
UGC 5101	1342204962	6.071	0.039	2.327	0.018	0.746	0.009
Mrk 273	1342201217	4.190	0.011	1.493	0.006	0.471	0.006
IRAS 13120-5453	1342226970	12.097	0.036	4.441	0.010	1.355	0.006
NGC 6240	1342203586	5.166	0.029	2.031	0.009	0.744	0.008
Arp 220	1342188687	30.414	0.132	12.064	0.036	4.145	0.015

final point source calibrated spectra are produced in Jy as a function of frequency (GHz). In Figure 8 a summary of the final spectra for all HERUS targets is shown. The spectra are in the galaxy rest frame ordered by increasing redshift. Many lines are visible in the spectra: we overlay vertical lines for the ^{12}CO ladder transitions between CO(5–4) and CO(13–12) at 576–1496 GHz (519–200 μm).

3.4. Photometry of HERUS Sources

All SPIRE photometry observations (listed in Table 1) were processed through the standard Small Map User Pipeline with HIPE 11.2825, using SPIRE Calibration Tree 11.0 with default values for all pipeline tasks. Target positions in the map were found by the HIPE SUSSEXtractor task (Savage & Oliver 2007), assuming an FWHM of 18.¹⁵, 25.², and 36.⁹ for the PSW, PMW, and PLW bands, respectively. These positions were then

input into the SPIRE Timeline Fitter task within HIPE (Pearson et al. 2014) that fits a Gaussian function to the baseline-subtracted SPIRE timelines. The background is measured within an annulus between 300 and 350 arcsec and then an elliptical Gaussian function is fit to both the central 22'', 32'', and 40'' (for the PSW, PMW, and PLW bands, respectively) and the background annulus. The results for the photometry of all the HERUS galaxies are shown in Table 2. Full details will be given in D.L. Clements et al. (2016, in preparation).

4. LINE FITTING

4.1. Fitting Lines to the Data

Line fitting to our final spectra is carried out using a dedicated line-fitting algorithm for the SPIRE FTS within the HIPE framework. The task does not search for lines but rather fits spectral features at expected line positions. The task

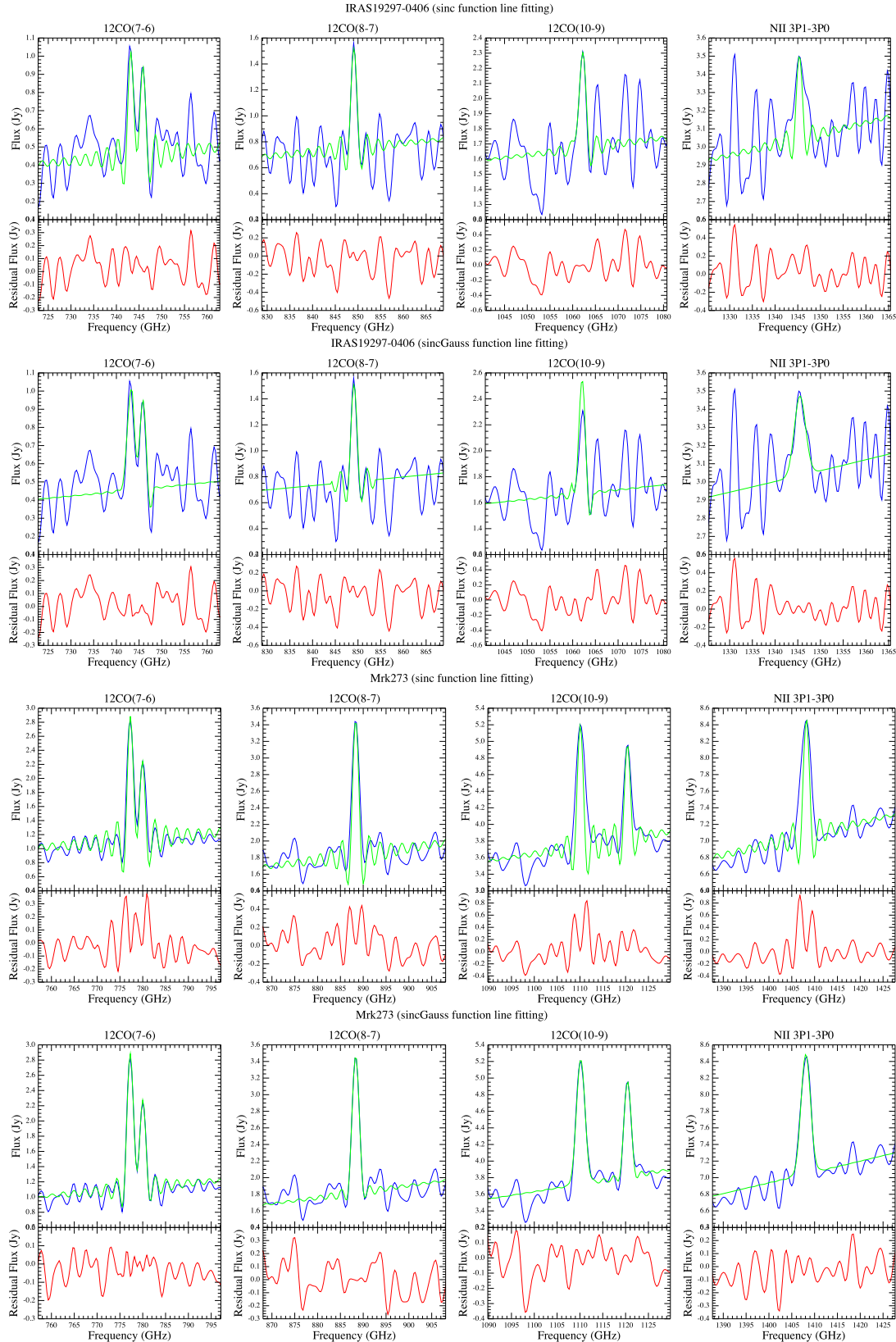


Figure 9. Line-fitting results for IRAS 19297-0406 (top rows) and Mrk 273 (bottom rows). Blue lines are the final spectra, green lines are the fit, and red lines are the residual after model fit subtraction. The top panel shows an example where the sinc-fit to the CO lines has been made. The lower panels for each object show an example where the sinc-Gauss-fit to the CO lines has been made. For IRAS 19297-0406, the sinc-fit is better than the sinc-Gauss-fit. For Mrk 273, the sinc-Gauss-fit produces a better fit. Note that in both cases the sinc-Gauss profile provides a better fit to [N II] 205 μm .

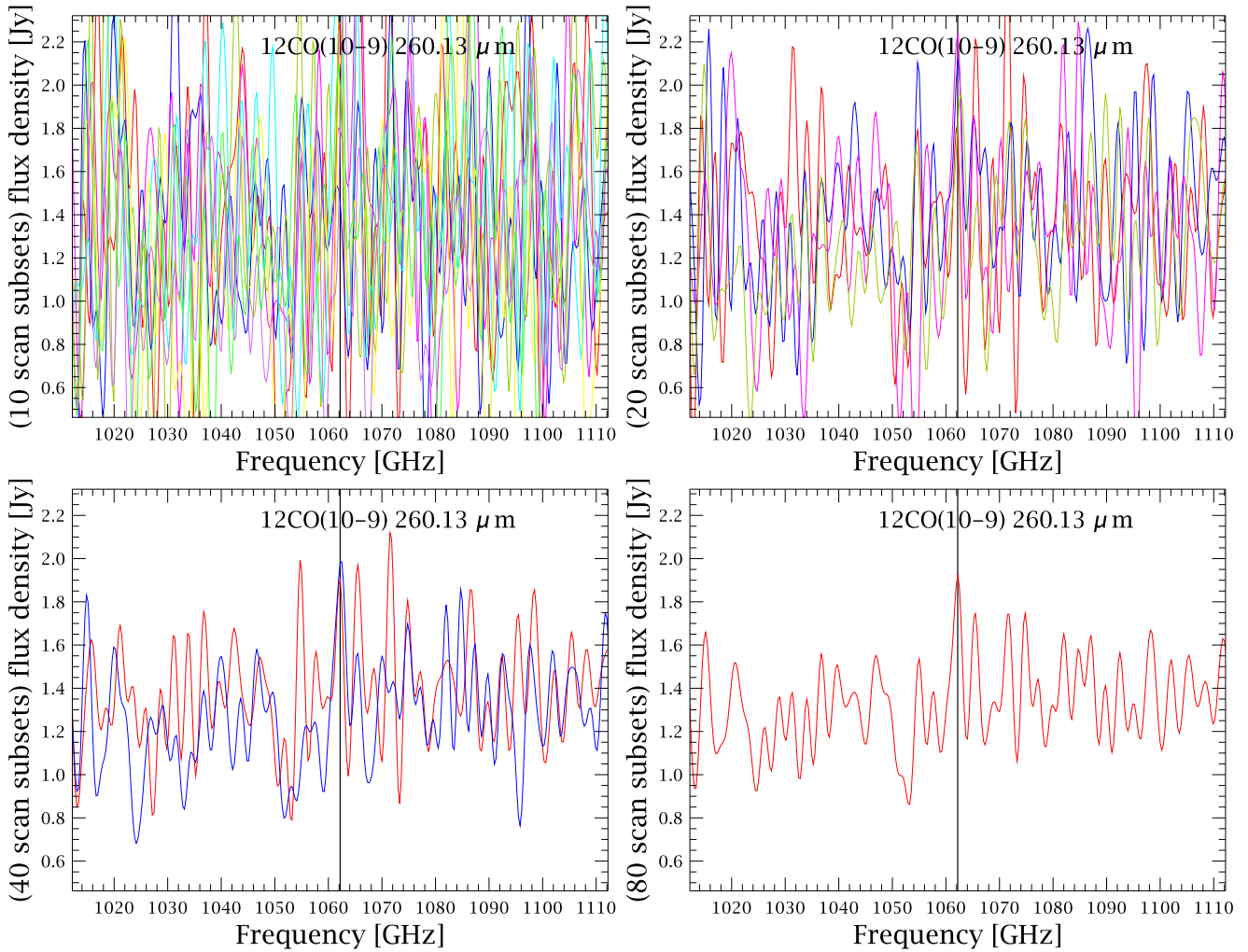


Figure 10. Example of a jack knife test for the CO(10–9) line, for IRAS 19297–0406. The total number of FTS scans is 80 and subsets of 60, 40, 30, 20, and 10 averaged scans are created. Except for the lowest subset of 10 scans, CO(10–9) is seen in all scans in all subsets (only the subsets 10, 20, 40, and 80 are shown in the figure), implying a robust detection of the line. The jack knife test can be used to distinguish between real detections such as the redshifted CO(10–9) line around 1060 GHz and spurious artifacts such as the line around 1055 GHz.

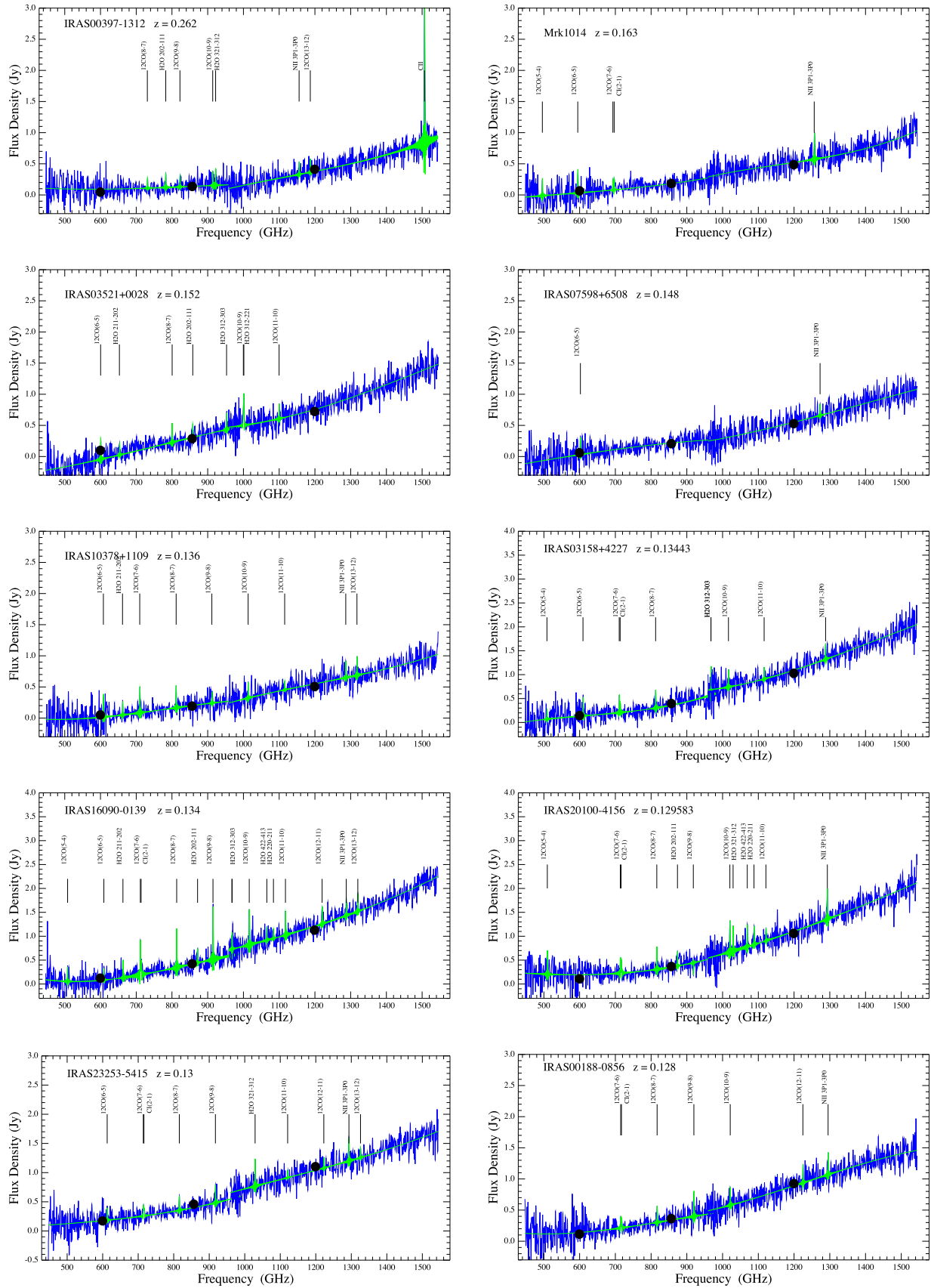
performs a global fit to a specified list of lines in the Level 2 point-source-calibrated spectrum using the HIPE Spectrum Fitter (a dedicated spectrum fitting Java task within HIPE).

Since the Spectrum Fitter task makes a global fit for all lines, the results were found to be sensitive to the number of input lines to the fit. Therefore it was found that the best way to run this fitter followed an iterative approach where a long list of lines for the initial fit was used. The resulting fits were then inspected visually. Lines that were clearly not real were discarded from the input file. The Spectrum Fitter was then run again on the reduced set of lines to produce a final list of measurements. This method does not find lines that are not in the original input table, but no such lines were apparent from visual inspection. The errors on the line fluxes are provided by the HIPE line fitter task as the standard deviation on the fit (assuming a sinc function using the Levenberg-Marquardt algorithm). Note that there is an additional systematic error component of 2.6% due to the line asymmetry caused by a residual phase shift in the interferogram (Hopwood et al. 2015).

The FTS instrument line shape can be approximated by a sinc function (Swinyard et al. 2014; Hopwood et al. 2015); however, for partially resolved lines, a sinc-Gaussian may be more

appropriate. Most line widths for our sources were well fitted by the sinc function and have widths of less than $\sim 300 \text{ km s}^{-1}$. In principle the resolution at the highest frequencies is comparable with some of the ground-based measurements but we see very few cases where an alternative sinc-Gauss improves the CO data. In Figure 9 the effectiveness of the sinc profile fit for the HERUS ULIRGs is shown for two examples, IRAS 19297–0406 and Mrk 273. For IRAS 19297–0406, the profiles for the CO(7–6), CO(8–7) and CO(10–9) lines are all well fitted by the sinc function, with the sinc-Gauss overestimating the peak flux for the CO(10–9) line. For Mrk 273, the CO(10–9) line and possibly the CO(8–7) line appear partially resolved and the sinc-Gauss profile provides a better fit. Note, however, that this line may suffer contamination from an H₂O line (H₂O 3_12–2_21 on the blue side of the CO line), which could broaden the ²CO(10–9) line (González-Alfonso et al. 2010, 2014). In both cases a broad N II line at 205 μm (1461 GHz) is present and is better fit by the sinc-Gauss profile.

We obtain a measure of the signal-to-noise of the line detection by using the residual of the continuum fit to the final spectrum (calculated by the line-fitting task; see the lower panels in each plot of Figure 9). By selecting an appropriate



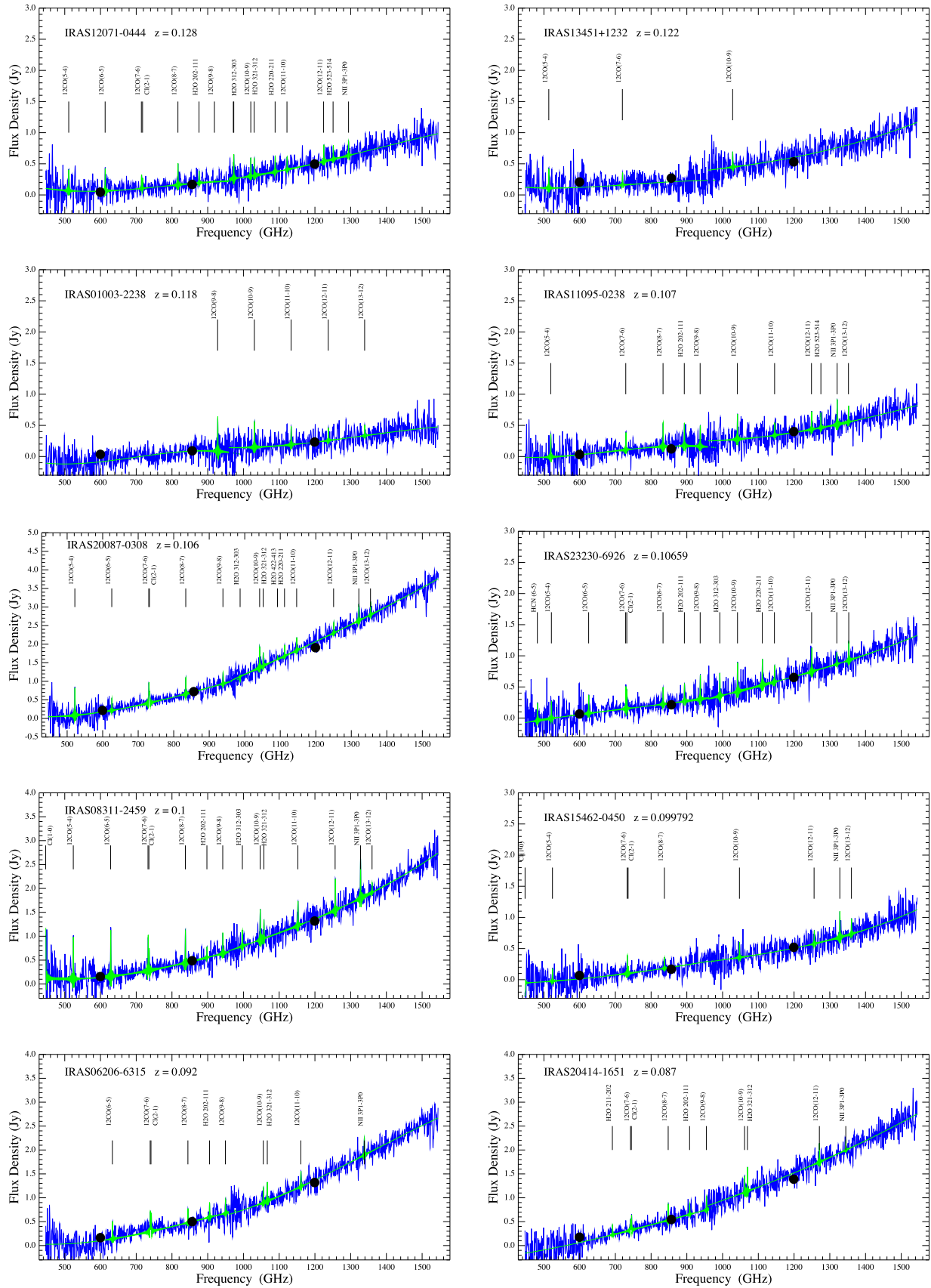


Figure 12. Line-fitting results for IRAS 12071-0444, IRAS 13451+1232, IRAS 01003-2238, IRAS 11095-0238, IRAS 20087-0308, IRAS 23230-6926, IRAS 08311-2459, IRAS 15462-0450, IRAS 06206-6315, and IRAS 20414-1651. The processed spectra (blue) are shown with the model fits overlaid (green). Photometry points are also shown (black dots). Fitted line species are indicated by the vertical bars.

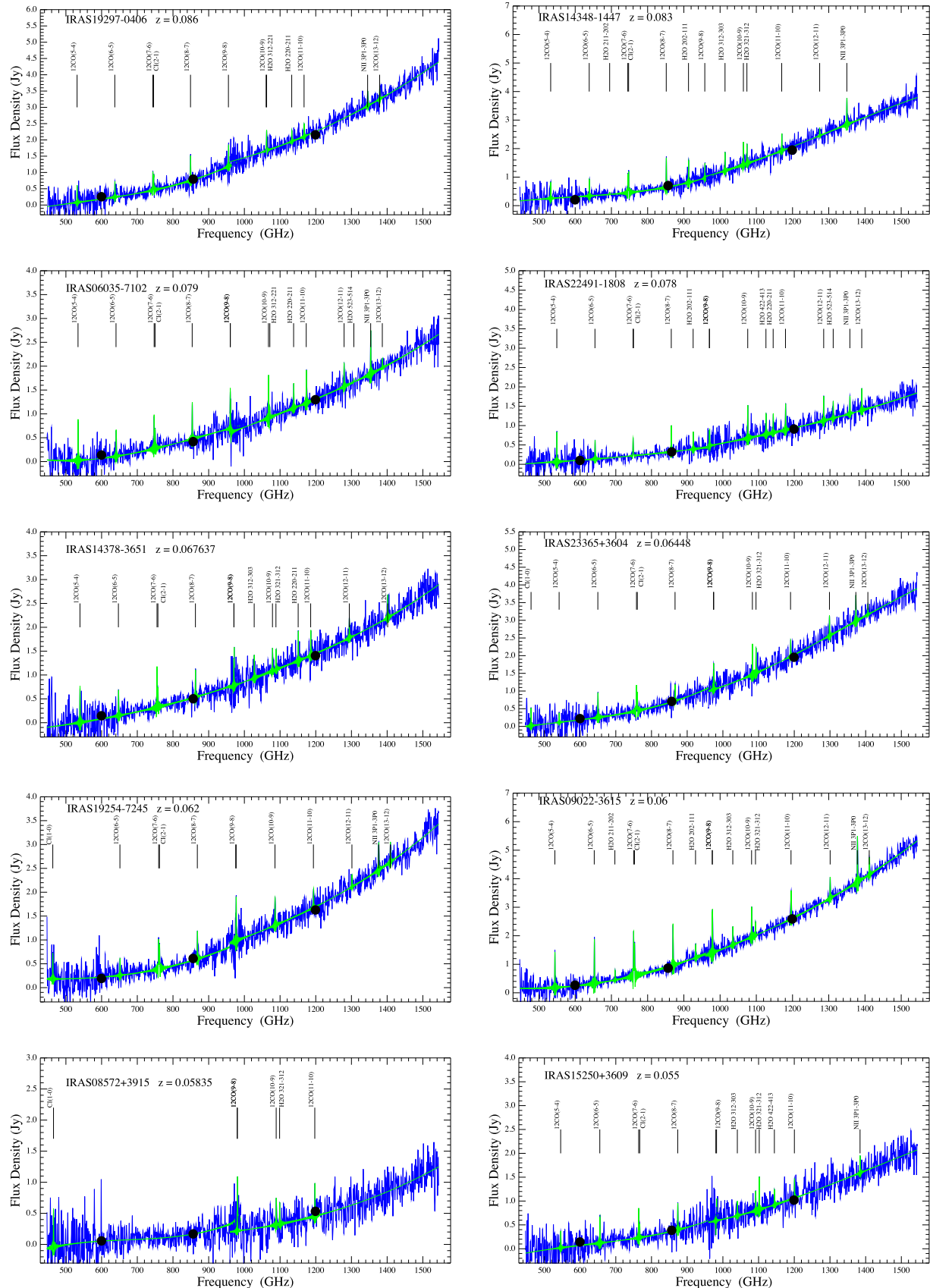


Figure 13. Line-fitting results for IRAS 19297–0406, IRAS 14348–1447, IRAS 06035–7102, IRAS 22491–1808, IRAS 14378–3651, IRAS 23365+3604, IRAS 19254–7245, IRAS 09022–3615, IRAS 08572+3915, and IRAS 15250+3609. The processed spectra (blue) are shown with the model fits overlaid (green). Photometry points are also shown (black dots). Fitted line species are indicated by the vertical bars.

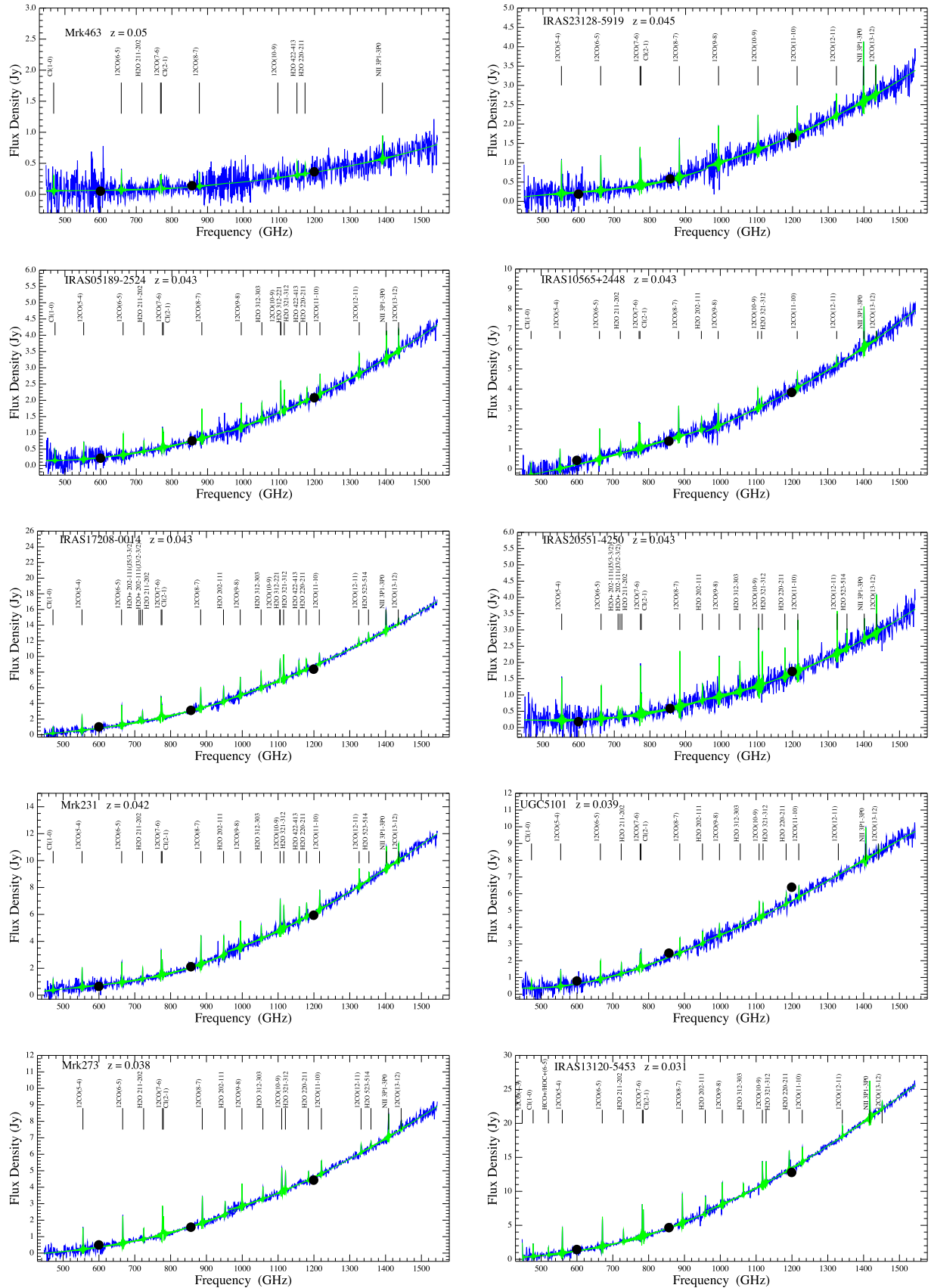


Figure 14. Line-fitting results for Mrk 463, IRAS 23128–5919, IRAS 05189–2524, IRAS 10565+2448, IRAS 17208–0014, IRAS 20551–4250, Mrk 231, UGC 5101, Mrk 273, and IRAS 13120–5453. The processed spectra (blue) are shown with the model fits overlaid (green). Photometry points are also shown (black dots). Fitted line species are indicated by the vertical bars.

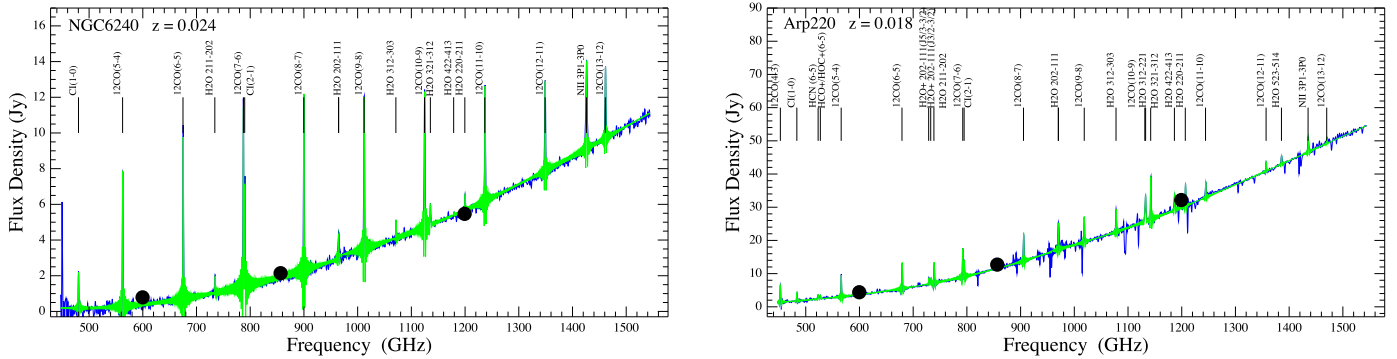


Figure 15. Line-fitting results for NGC 6240 and Arp 220. The processed spectra (blue) are shown with the model fits overlaid (green). Photometry points are also shown (black dots). Fitted line species are indicated by the vertical bars.

frequency range around the line of interest (50 spectral pixels around the line), the standard deviation of the residual in that range is calculated. The signal to noise is then estimated by dividing the fitted line height (i.e., peak flux) by the standard deviation of the residual.

4.2. Jack Knife Tests

Many of the objects of the HERUS sample are considered faint sources for the SPIRE FTS ($250\text{ }\mu\text{m}$ flux density $<500\text{ mJy}$) and the corresponding line detections are often $<5\sigma$. In order to differentiate a true line detection from spurious detections manifested by low-frequency noise in the FTS spectrum, a Jack Knife test was performed to confirm statistically robust detections of the lines.

The jack knife tests can be performed by either treating the forward and reverse scans of the FTS separately or by dividing the total number of scans into smaller subsets. For our data we perform jack knife tests by first dividing the total number of scans into two subsets and then consecutively halving the subsets to create further subsets (i.e., for an observation with a total of 200 scans, it is first divided into two subsets of 100 scans, then 4 subsets of 50, down to subsets of 10 scans). Visually inspecting plots of the scan subsets allows confirmation of the existence of a line. The smallest subsets should be indistinguishable from noise unless there is some systematic noise manifesting as a line detection. Increasing the number of scan lines per subset should highlight any real line, while the surrounding samples around the line are still consistent with noise. Using this method a statistically robust selection of lines can be realized. The jack knife test for the CO(10–9) line in IRAS 19297-0406 is shown in Figure 10, which shows results for scan subsets of 80, 40, 20, and 10 FTS scans. The CO(10–9) is seen in all scans in all subsets, except for the lowest 10 scan subset plot, giving us confidence in the detection of the line.

5. RESULTS

5.1. Fitted Spectra

The final spectra for each ULIRG are shown in Figures 11–15. The galaxies are tabulated in order of decreasing redshift, beginning with IRAS 00397-1312 at $z = 0.262$, to Arp 220 at $z = 0.018$. The final concatenated spectra for the SSW and SLW bands are plotted as flux density (Jy) as a function of frequency (GHz). Overlaid on the spectra are the SPIRE photometry points and the fitted lines as described in Section 4.

For our highest-redshift object, IRAS 00397-1312 at $z = 0.262$, the [C II] line at $157.7\text{ }\mu\text{m}$ is redshifted into the SPIRE FTS SSW band pass. For this source a line flux of $28.22 \pm 0.81 \times 10^{-18}\text{ Wm}^{-2}$ is measured, corresponding to a line luminosity of $10^{9.20 \pm 0.07} L_{\odot}$, a value comparable with similar ULIRGs at similar redshift (e.g., Magdis et al. 2014).

CO lines are prominent in the majority of our sources. For two of our sources, IRAS 13120-5453 and Arp 220, the CO(4–3) transition at 461 GHz (649 μm) is also detected. Some sources, notably IRAS 07598+6508 ($z = 0.148$), Mrk 1014 ($z = 0.163$), IRAS 13451+1232 ($z = 0.122$) and IRAS 08572+3915 ($z = 0.058$), do not show CO lines. These sources are associated with AGN/BAL QSOs (Lipari 1994; Boller et al. 2002; Spoon et al. 2009). Note that the FTS spectrum of IRAS 08572+3915 has been reported in Efstathiou et al. (2014) and was modeled with an edge-on AGN torus.

The CO line fluxes for our sample are given in Table 3. Comparing our results with published ULIRGs, we find good agreement within the errors for Arp 220 (Rangwala et al. 2011) and Mrk 231 (van der Werf et al. 2010). In the case of NGC 6240 we measure substantially lower line fluxes compared to Meijerink et al. (2013). The reason for this discrepancy is unclear since it is the same observation, although the data presented in Meijerink et al. (2013) were processed with an earlier version of the FTS pipeline (HIPE version 6.0).

In addition, in many sources we detect the two [C I] fine structure lines at 492 GHz (607 μm) and 809 GHz (370 μm), originating in photodissociation regions in the transition region between the ionized carbon and molecular CO (Kaufman et al. 1999). Moreover, the [N II] 3P1-3P0 fine structure line at 1461 GHz (205 μm) is detected for the majority of the sample. The [N II] line is indicative of hot HII regions rather than the PDR and can be used to estimate the fraction of [C II] emission that comes from ionized gas, rather than from PDRs. In many cases, the [N II] line is partially resolved and relatively broad (see Figure 9) and a sinc-Gauss profile was used to model the line in many instances where FWHM of $\sim 300\text{--}400\text{ km s}^{-1}$ were measured. Although broad, these widths are still significantly smaller than those in systems that unambiguously are shown to have massive outflows (e.g., Feruglio et al. 2010; Cicone et al. 2014).

Water is the second most oxygenated molecule (following CO) in the warm interstellar medium of galaxies and has been detected by *Herschel* in observations of nearby ULIRGs (González-Alfonso et al. 2010; Rangwala et al. 2011; Pereira-Santalla et al. 2013). The HERUS ULIRGs are also found to be abundant in water lines, in particular the ortho-H₂O lines,

Table 3
 ^{12}CO Line Fluxes as Measured by the SPIRE FTS

Transition ν_{rest} (GHz)	5–4 576.3	6–5 691.5	7–6 806.7	8–7 921.8	9–8 1036.9	10–9 1151.9	11–10 1267.0	12–11 1382.0	13–12 1496.9
Name	$10^{-18} \text{ W m}^{-2}$								
IRAS 00397-1312	4.05 ± 0.80	2.51 ± 0.78	...	1.91 ± 0.78	2.07 ± 0.79	2.67 ± 0.79	2.54 ± 0.80
Mrk 1014	3.33 ± 0.75	4.56 ± 0.75	1.96 ± 0.76	– ± –
IRAS 03521+0028	...	4.11 ± 0.78	...	3.65 ± 0.78	...	4.46 ± 0.87	2.85 ± 0.78	2.21 ± 0.78	...
IRAS 07598+6508	...	3.30 ± 0.78	...	– ± –
IRAS 10378+1109	...	4.42 ± 0.76	4.92 ± 0.76	4.24 ± 0.76	2.15 ± 0.76	3.02 ± 0.70	1.67 ± 0.70	...	3.59 ± 0.70
IRAS 03158+4227	2.61 ± 0.94	4.69 ± 0.94	4.31 ± 0.96	4.49 ± 0.94	...	4.33 ± 0.91	2.90 ± 0.91
IRAS 16090-0139	3.68 ± 0.09	2.93 ± 0.85	9.25 ± 8.94	9.74 ± 0.85	13.20 ± 0.85	8.91 ± 0.85	5.88 ± 0.84	4.24 ± 0.84	4.40 ± 0.84
IRAS 20100-4156	5.92 ± 0.96	...	4.08 ± 1.00	5.63 ± 0.96	...	8.10 ± 0.99	3.22 ± 0.99
IRAS 23253-5415	...	2.57 ± 0.73	2.63 ± 0.75	2.99 ± 0.73	3.73 ± 0.73	...	1.49 ± 0.77	2.15 ± 0.77	2.06 ± 0.77
IRAS 00188-0856	2.39 ± 0.89	3.12 ± 0.85	4.83 ± 0.85	3.45 ± 0.73	...	3.62 ± 0.73	...
IRAS 12071-0444	3.64 ± 0.76	4.46 ± 0.76	2.35 ± 0.77	3.80 ± 0.76	0.00 ± 0.76	3.69 ± 0.71	2.04 ± 0.71	2.56 ± 0.71	...
IRAS 13451+1232	3.69 ± 0.90	...	2.41 ± 0.89	– ± –	...	2.96 ± 0.82
IRAS 01003-2238	– ± –	6.61 ± 0.82	0.00 ± 0.75	3.52 ± 0.75	2.42 ± 0.75	2.05 ± 0.75
IRAS 11095-0238	4.39 ± 0.82	...	3.32 ± 0.82	4.68 ± 0.82	4.10 ± 0.83	4.87 ± 0.80	2.43 ± 0.80	0.00 ± 0.80	3.06 ± 0.80
IRAS 20087-0308	8.79 ± 0.90	3.96 ± 0.90	7.52 ± 0.93	5.37 ± 0.90	3.70 ± 0.90	6.52 ± 0.88	4.18 ± 0.88	0.00 ± 0.88	4.11 ± 0.88
IRAS 23230-6926	3.37 ± 0.83	0.83 ± 0.83	3.96 ± 0.84	3.24 ± 0.83	4.70 ± 0.83	5.53 ± 0.78	3.15 ± 0.78	4.54 ± 0.78	3.63 ± 0.78
IRAS 08311-2459	10.50 ± 1.00	11.50 ± 1.00	8.54 ± 1.03	8.05 ± 1.00	5.19 ± 1.00	7.55 ± 0.90	6.13 ± 0.92	7.86 ± 0.92	2.53 ± 0.92
IRAS 15462-0450	2.40 ± 0.81	...	3.48 ± 0.82	2.07 ± 0.81	...	2.91 ± 0.74	...	2.54 ± 0.74	0.00 ± 0.74
IRAS 06206-6315	...	4.40 ± 0.94	5.26 ± 0.99	3.54 ± 0.94	3.45 ± 0.94	3.91 ± 0.82	3.86 ± 0.82
IRAS 20414-1651	2.62 ± 0.97	3.96 ± 0.93	3.35 ± 0.93	3.89 ± 0.91	...	4.66 ± 0.90	...
IRAS 19297-0406	6.23 ± 1.14	5.72 ± 1.14	6.72 ± 1.19	9.19 ± 1.14	7.82 ± 1.15	2.77 ± 0.13	4.64 ± 0.12	...	4.32 ± 1.16
IRAS 14348-1447	6.90 ± 1.09	7.07 ± 0.11	7.87 ± 1.14	11.20 ± 1.09	6.33 ± 1.10	9.32 ± 0.11	7.23 ± 0.11	3.33 ± 0.11	...
IRAS 06035-7102	10.20 ± 1.00	6.58 ± 1.00	8.05 ± 1.02	9.15 ± 1.00	10.10 ± 0.99	2.91 ± 0.96	8.40 ± 0.95	5.87 ± 0.95	2.47 ± 0.95
IRAS 22491-1808	9.14 ± 0.88	5.69 ± 0.88	5.42 ± 1.13	8.20 ± 0.88	5.57 ± 0.89	10.20 ± 0.96	8.07 ± 0.98	7.48 ± 0.98	6.76 ± 0.99
IRAS 14378-3651	9.03 ± 1.16	6.47 ± 1.16	9.89 ± 1.20	6.80 ± 1.16	6.88 ± 1.11	5.63 ± 1.10	6.41 ± 1.09	5.13 ± 1.09	5.78 ± 1.09
IRAS 23365+3604	3.20 ± 1.11	8.45 ± 1.11	8.74 ± 1.16	5.56 ± 1.11	6.29 ± 1.12	10.10 ± 1.11	5.55 ± 1.11	6.73 ± 1.11	3.39 ± 1.11
IRAS 19254-7245	...	4.36 ± 1.06	7.75 ± 1.11	6.97 ± 1.06	7.97 ± 1.07	6.97 ± 1.00	4.75 ± 1.00	3.07 ± 1.00	5.07 ± 1.00
IRAS 09022-3615	15.00 ± 1.02	18.60 ± 1.02	19.80 ± 1.07	17.80 ± 1.02	17.70 ± 1.04	12.80 ± 0.98	11.90 ± 0.98	8.93 ± 0.98	7.37 ± 0.98
IRAS 08572+3915	– ± –	8.64 ± 1.17	5.12 ± 1.10	6.33 ± 1.10
IRAS 15250+3609	4.17 ± 1.16	6.55 ± 1.16	7.07 ± 1.17	6.64 ± 1.16	4.71 ± 1.17	4.68 ± 1.17	4.96 ± 1.16
Mrk 463	...	3.79 ± 0.80	3.04 ± 0.86	2.63 ± 0.82	...	1.52 ± 0.75
IRAS 23128-5919	10.40 ± 0.94	10.80 ± 0.94	15.60 ± 0.97	11.90 ± 0.94	11.70 ± 0.99	10.70 ± 0.99	8.69 ± 0.96	6.72 ± 0.99	9.01 ± 9.86
IRAS 05189-2524	4.71 ± 0.93	6.44 ± 0.93	7.93 ± 0.97	9.90 ± 0.93	9.95 ± 0.85	12.60 ± 1.23	9.15 ± 0.85	7.57 ± 0.85	7.32 ± 0.85
IRAS 10565+2448	11.70 ± 1.37	18.30 ± 1.37	14.10 ± 1.40	18.40 ± 1.37	13.40 ± 1.26	11.90 ± 1.26	9.56 ± 1.25	4.92 ± 1.25	4.78 ± 1.25
IRAS 17208-0014	22.60 ± 1.43	30.40 ± 1.43	31.70 ± 1.50	32.20 ± 1.43	27.80 ± 1.57	28.70 ± 1.67	15.90 ± 1.56	9.99 ± 1.56	8.72 ± 1.56
IRAS 20551-4250	15.50 ± 1.18	12.40 ± 1.18	17.70 ± 1.22	20.40 ± 1.18	14.60 ± 1.12	20.70 ± 1.12	18.80 ± 1.12	15.60 ± 1.12	13.80 ± 1.12
Mrk 231	17.40 ± 1.22	17.30 ± 1.22	21.80 ± 1.26	25.80 ± 1.22	22.80 ± 1.21	26.50 ± 1.21	17.20 ± 1.20	15.50 ± 1.21	15.00 ± 1.21
UGC 5101	11.70 ± 1.25	13.30 ± 1.25	9.55 ± 1.30	11.00 ± 1.25	8.19 ± 1.38	12.00 ± 1.38	8.25 ± 1.37	2.46 ± 1.37	5.25 ± 1.37
Mrk 273	15.70 ± 0.82	20.00 ± 0.82	21.00 ± 0.86	19.50 ± 0.82	16.20 ± 0.95	17.00 ± 0.95	9.37 ± 0.95	6.30 ± 0.95	6.82 ± 0.95
IRAS 13120-5453 ^a	45.30 ± 1.69	51.20 ± 1.69	53.60 ± 1.74	51.00 ± 1.69	38.30 ± 1.76	39.70 ± 1.76	26.10 ± 1.76	17.90 ± 1.76	14.10 ± 1.76
NGC 6240	94.80 ± 2.75	107.00 ± 2.75	122.00 ± 2.86	121.00 ± 2.75	102.00 ± 2.82	94.20 ± 2.82	81.00 ± 2.81	63.50 ± 2.82	51.70 ± 2.82
Arp 220 ^b	76.70 ± 4.08	95.20 ± 4.07	99.00 ± 4.20	97.30 ± 4.08	90.10 ± 6.82	70.10 ± 7.56	55.20 ± 6.81	32.90 ± 6.81	22.10 ± 6.82

Notes.

^a Also: CO(4-3) flux of $25.6 \pm 2.2 \times 10^{-18} \text{ W m}^{-2}$.

^b Also: CO(4-3) flux of $62.4 \pm 4.15 \times 10^{-18} \text{ W m}^{-2}$.

Table 4
H₂O Line Fluxes as Measured by the SPIRE FTS

Transition ν_{rest} (GHz)	2 ₁₁ –2 ₀₂ 752.0	2 ₀₂ –1 ₁₁ 987.9	3 ₁₂ –3 ₀₃ 1097.4	3 ₁₂ –2 ₂₁ 1153.1	3 ₂₁ –3 ₁₂ 1162.9	4 ₂₂ –4 ₁₃ 1207.6	2 ₂₀ –2 ₁₁ 1228.8	5 ₂₃ –5 ₁₄ 1410.6
Name	$10^{-18} \text{ W m}^{-2}$							
IRAS 00397-1312	...	2.79 ± 0.78	3.20 ± 0.79	3.20 ± 0.79
Mrk 1014
IRAS 03521+0028	...	2.58 ± 0.77	3.23 ± 0.78	3.23 ± 0.78
IRAS 07598+6508
IRAS 10378+1109	2.62 ± 0.76
IRAS 03158+4227	7.17 ± 0.95	7.17 ± 0.95
IRAS 16090-0139	4.43 ± 0.85	3.52 ± 0.85	4.88 ± 0.86	4.88 ± 0.86	...	3.44 ± 0.84
IRAS 20100-4156	...	3.59 ± 0.96	6.72 ± 0.99	5.69 ± 0.99	4.75 ± 0.99	...
IRAS 23253-5415	5.57 ± 0.77
IRAS 00188-0856
IRAS 12071-0444	4.63 ± 0.72	4.63 ± 0.72	2.88 ± 0.71	...	3.02 ± 0.71	3.27 ± 0.71
IRAS 13451+1232
IRAS 01003-2238
IRAS 11095-0238	4.41 ± 0.82
IRAS 20087-0308	4.10 ± 0.88	...	3.51 ± 0.88	...
IRAS 23230-6926	...	3.44 ± 0.83	4.35 ± 0.78	4.35 ± 0.78	4.97 ± 0.78	...
IRAS 08311-2459	3.99 ± 0.92	3.99 ± 0.92	4.53 ± 0.92
IRAS 15462-0450
IRAS 06206-6315	...	3.73 ± 0.94
IRAS 20414-1651	5.85 ± 0.91
IRAS 19297-0406	7.90 ± 1.29
IRAS 14348-1447	...	9.33 ± 1.09	7.68 ± 1.06	...	8.10 ± 1.06
IRAS 06035-7102	11.0 ± 0.96	6.35 ± 0.95	...
IRAS 22491-1808	...	5.35 ± 0.88	6.40 ± 0.99	6.04 ± 0.99	5.22 ± 0.98
IRAS 14378-3651	5.84 ± 1.10	...	4.95 ± 1.10	...	7.45 ± 1.09	...
IRAS 23365+3604	8.24 ± 1.11
IRAS 19254-7245
IRAS 09022-3615	4.16 ± 1.02	5.44 ± 1.03	7.82 ± 0.98	5.61 ± 0.98
IRAS 08572+3915
IRAS 15250+3609	8.06 ± 1.17	3.87 ± 1.16
Mrk 463
IRAS 23128-5919
IRAS 05189-2524	3.74 ± 0.93	...	7.56 ± 0.85	5.17 ± 1.22	6.29 ± 0.86	3.91 ± 0.85	6.68 ± 0.86	...
IRAS 10565+2448	6.88 ± 1.37	7.81 ± 1.37
IRAS 17208-0014 ^a	16.40 ± 1.44	23.50 ± 1.44	24.70 ± 1.56	34.6 ± 1.67	38.30 ± 1.57	19.20 ± 1.57	16.00 ± 1.56	11.40 ± 1.60
IRAS 20551-4250	...	5.91 ± 1.18	10.90 ± 1.12	...	11.70 ± 1.12	...	10.40 ± 1.12	7.19 ± 1.12
Mrk 231	9.76 ± 1.22	15.50 ± 1.22	11.90 ± 1.21	...	19.60 ± 1.21	12.40 ± 1.20	12.70 ± 1.20	6.70 ± 1.21
UGC 5101	7.66 ± 1.25	8.47 ± 1.21	3.94 ± 1.37	...	9.35 ± 1.38	...	9.01 ± 1.37	...
Mrk 273	7.95 ± 0.82	9.86 ± 0.83	8.88 ± 0.95	...	12.90 ± 0.95	...	5.88 ± 0.95	4.56 ± 0.95
IRAS 13120-5453	20.90 ± 1.69	28.80 ± 1.70	19.70 ± 1.76	...	36.20 ± 1.76	...	34.10 ± 1.77	...
NGC 6240	14.70 ± 2.75	14.80 ± 2.87	11.00 ± 2.82	...	13.00 ± 2.80	5.42 ± 2.82	12.70 ± 2.80	...
Arp 220 ^b	75.10 ± 4.10	96.90 ± 4.11	80.30 ± 6.81	97.3 ± 7.58	155.00 ± 6.84	58.60 ± 6.81	78.80 ± 6.81	31.50 ± 6.80

Notes.

^a Also: H₂O⁺ 2₀₂–1_{11(J5/3–3/2)} and H₂O⁺ 2₀₂–1_{11(J3/2–3/2)} fluxes of 7.15 ± 1.45 and 6.28 ± 1.40 × 10⁻¹⁸ W m⁻², respectively.

^b Also: H₂O⁺ 2₀₂–1_{11(J5/3–3/2)} and H₂O⁺ 2₀₂–1_{11(J3/2–3/2)} fluxes of 22.0 ± 4.12 and 21.2 ± 4.14 × 10⁻¹⁸ W m⁻², respectively.

H₂O 3₁₂–3₀₃ at 1097 GHz (272 μm), H₂O 3₁₂–2₂₁ at 1153 GHz (259 μm), H₂O 3₂₁–3₁₂ at 1163 GHz (257 μm), H₂O 5₂₃–5₁₄ at 1411 GHz (212 μm), H₂O+2₀₂–1_{11(J5/3–3/2)} at 742 GHz (404 μm), H₂O+2₀₂–1_{11(J3/2–3/2)} at 746 GHz (401 μm) and the para-H₂O lines, H₂O 2₀₂–1₁₁ at 988 GHz (303 μm), H₂O 4₂₂–4₁₃ at 1208 GHz (248 μm), and H₂O 2₂₀–2₁₁ at 1229 GHz (243 μm). The strength of the water lines can vary considerably from source to source; there are examples where the water lines have a similar emission strength to the CO lines (IRAS 12071-0444, IRAS 23230-6926, IRAS 06206-6315), and where the water lines, although detected, are significantly weaker than the CO

lines (IRAS 09022-3615, IRAS 10565+2448, NGC 6240). A thorough investigation of the water emission in the HERUS sample is beyond the scope of the current work and will be reported on in a forthcoming paper; however, we note that our measured fluxes for the water lines in Mrk 231 and Arp 220 are consistent within the errors with the results of González-Alfonso et al. (2010, 2013).

Finally, in addition to the above species, we also detect HCO⁺/HOC^{+(6–5)} at 537 GHz (557 μm) in IRAS 13120–5453, and confirm the detection of both HCO⁺/HOC⁺ and HCN at 532 GHz (562 μm) in Arp 220 Rangwala et al. (2011).

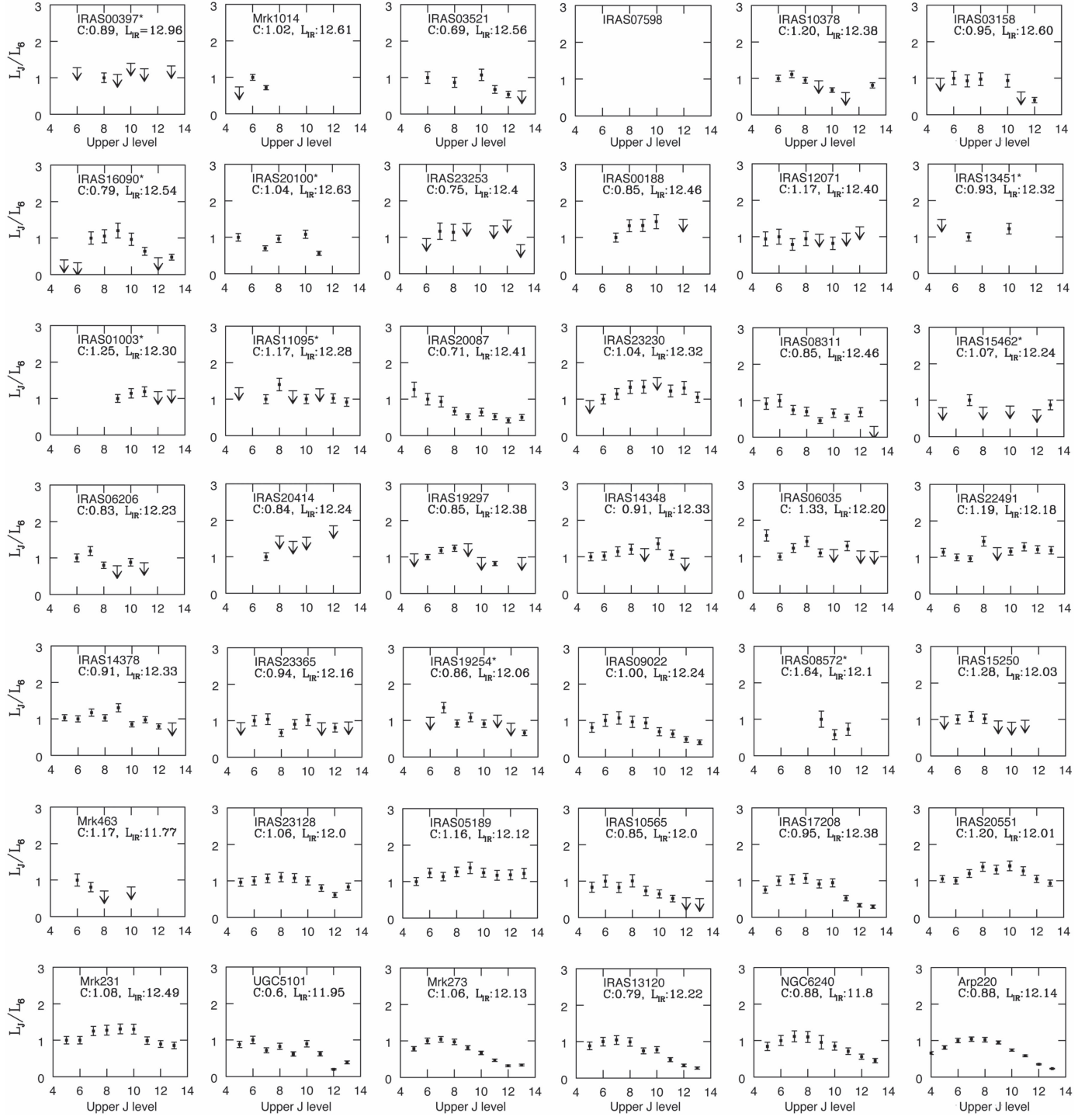


Figure 16. CO SLEDs for HERUS galaxies ordered by decreasing redshift as in Figures 11–15. The line luminosity normalized to the $L_{CO(6-5)}$ luminosity is plotted against transition level (J) for all sources, unless marked with an asterisk; then the CO(7–6) or higher transition is used. Also shown is the infrared color given by the $IRAS$ flux ratio $C_2 = S_{60}/S_{100}$.

In Table 4 the water line fluxes as measured by the SPIRE FTS for the HERUS local ULIRGs are tabulated in units of $10^{-18} \text{ W m}^{-2}$. Line flux estimates were only included for cases where the measured signal to noise of the water lines was $>3\sigma$.

5.2. CO SLED Modeling

In Figure 16 we plot the CO SLEDs for HERUS galaxies ordered by decreasing redshift in the same order as Figures 11–

15. For each galaxy the L_J line luminosity normalized to the $L_{CO(6-5)}$ luminosity is plotted against transition level (J). When the $L_{CO(6-5)}$ line luminosity is not available, the luminosity is normalized to the $L_{CO(7-6)}$ or that of a higher transition. The $L_{CO(6-5)}$ was chosen because the CO(6–5) transition is the most commonly detected line in the HERUS sample. Note that there is no SLED for IRAS 07598+6508, since only a single CO line (CO(6–5)) was detected.

Table 5

Infrared Colors of HERUS ULIRGs Derived from *IRAS* Fluxes at 25 μm ,
60 μm , and 100 μm

Target	C1 S_{25}/S_{60}	C2 S_{60}/S_{100}
IRAS 00397-1312	0.31	0.88
Mrk 1014	0.27	1.02
3C273	0.42	0.76
IRAS 03521+0028	0.09	0.69
IRAS 07598+6508	0.35	0.94
IRAS 10378+1109	0.15	1.20
IRAS 03158+4227	0.11	0.95
IRAS 16090-0139	0.07	0.79
IRAS 20100-4156	0.08	1.04
IRAS 23253-5415	0.10	0.76
IRAS 00188-0856	0.23	0.85
IRAS 12071-0444	0.21	1.18
IRAS 13451+1232	0.33	0.94
IRAS 01003-2238	0.25	1.25
IRAS 23230-6926	0.09	1.04
IRAS 11095-0238	0.14	1.17
IRAS 20087-0308	0.06	0.71
IRAS 15462-0450	0.15	1.07
IRAS 08311-2459	0.22	0.86
IRAS 06206-6315	0.08	0.84
IRAS 20414-1651	0.09	0.89
IRAS 19297-0406	0.09	0.85
IRAS 14348-1447	0.08	0.91
IRAS 06035-7102	0.12	0.87
IRAS 22491-1808	0.10	1.19
IRAS 14378-3651	0.09	0.90
IRAS 23365+3604	0.11	0.94
IRAS 19254-7245	0.27	0.83
P09022-3615	0.10	1.00
IRAS 08572+3915	0.23	1.64
IRAS 15250+3609	0.18	1.28
Mrk 463	0.74	1.17
IRAS 23128-5919	0.15	1.06
IRAS 10565+2448	0.10	0.85
IRAS 20551-4250	0.15	1.20
IRAS 05189-2524	0.26	1.16
IRAS 17208-0014	0.05	0.95
Mrk 231	0.25	1.09
UGC 5101	0.09	0.60
Mrk 273	0.10	1.06
IRAS 13120-5453	0.07	0.79
NGC 6240	0.15	0.88
Arp 220	0.08	0.88

Note. Where C1 = S_{25}/S_{60} is used to differentiate between cold and hot sources and C2 = S_{60}/S_{100} can be used as a proxy for the temperature.

The ULIRG SLEDs in Figure 16 can be broadly grouped into three categories: flat, increasing (low to high J), and decreasing. The IR luminosity (reported in each SLED panel) is not a good indicator of the shape of the SLED. For example, IRAS 00188-0856 and IRAS 20087-0308 have similar L_{IR} but show very different SLEDs; the SLED of the former increases up to $J \sim 10$, while the latter peaks at $J \sim 5$.

Since the SLED of a galaxy represents the molecular gas mass distribution across a range of densities and temperatures (provided that the lines do not become optically thick), it is useful to look for possible dependencies of the shape of the SLED on these parameters. First, we investigate the

dependence of the shape of the SLED on the FIR color index C(60/100), which is a good proxy for the dust temperature (e.g., Rowan-Robinson & Crawford 1989). In addition we look for possible dependencies of the SLED on the $\alpha(25/60)$ color index, which has been widely used to differentiate between cold and warm ULIRGs (e.g., Sanders et al. 1988). Table 5 lists the infrared colors for all our sources, both the C(60/100) as well as $\alpha(25/60)$. For simplicity, we group FIR color indices according to their values: we classify C(60/100) > 1.0 as a warm color index, $0.6 < \text{C}(60/100) < 1.0$ as intermediate, and $\text{C}(60/100) < 0.6$ as cold. Following this scheme, we find that ULIRGs whose SLED increases with increasing J tend to have warm color indices, those with decreasing SLEDs (i.e., SLED peaking at $J \leq 6$) have cold color indices, and those displaying flat SLEDs have intermediate color indices. Thus, the shape of the SLED appears to be influenced by the physical properties (e.g., temperature) of the underlying radiation field, which was also noted by Lu et al. (2014) for their sample of LIRG galaxies. Finally, we note that an AGN (i.e., warm ULIRGs) will shift the peak of the SLED to higher J transitions, which may be a contributor to both higher C(60/100) colors and warmer SLEDs.

6. DISCUSSION

In order to probe the dependency of the shape of the SLED on the C(60/100) index further, in Figure 17 we plot the $L_{\text{CO}(1-0)}$, $L_{\text{CO}(6-5)}$, $L_{\text{CO}(9-8)}$, and $L_{\text{CO}(13-12)}$ line luminosities normalized by L_{IR} as a function of C(60/100) index. We focus on sources with firm detections in all CO transitions. ULIRGs where the fractional contribution of the AGN to the total bolometric output exceeds $\sim 40\%$ have been denoted with an open square and are not taken into account when estimating the slope of the correlation. The presence of an AGN with significant contribution to the total bolometric output was established based on the presence of [Ne V] $\lambda 14.32 \mu\text{m}$ or a very deep 9.7 μm silicate absorption feature (e.g., Farrah et al. 2007). Of the HERUS ULIRGs, six have AGN contributions $> 40\%$ (Desai et al. 2007; Farrah et al. 2007). The investigation of the SLED dependence on broadband colors is extended to SPIRE wavelengths in Figures 18 and 19, which again show the L_{CO} line luminosity normalized by L_{IR} , this time as a function of *IRAS/SPIRE* 100 $\mu\text{m}/250 \mu\text{m}$ and SPIRE 250 $\mu\text{m}/500 \mu\text{m}$ colors, respectively.

Figure 17 shows that as the C(60/100) index increases, the CO gas gets warmer. This is demonstrated by the inversion in the slopes of the linear fits to the data as a function of J , changing from -0.54 for the CO(1-0), through -0.2 for CO(6-5) and $+0.031$ for CO(9-8), to $+0.63$ for CO(12-11). The Pearson correlation coefficients confirm this: r is negative for CO(1-0), close to zero for CO(6-5) and CO(9-8), and positive for CO(12-11). The near-zero value ($r = 0.03$) computed for the mid- J transitions implies that the ratios $L_{\text{CO}(6-5)}/L_{\text{IR}}$ and $L_{\text{CO}(9-8)}/L_{\text{IR}}$ are constant over the values of the C(60/100) explored here. The scatter in the relations is also noteworthy. For the moderate J lines (6-5 and 9-8), the CO/ L_{IR} ratio has approximately the same value, with little scatter, for a wide range in S_{60}/S_{100} ratio. For the 1-0 and 12-11 lines, however, the CO/ L_{IR} ratio changes, and the scatter is greater. The same pattern is seen for the S_{100}/S_{250} ratio (Figure 18). Notably though, the

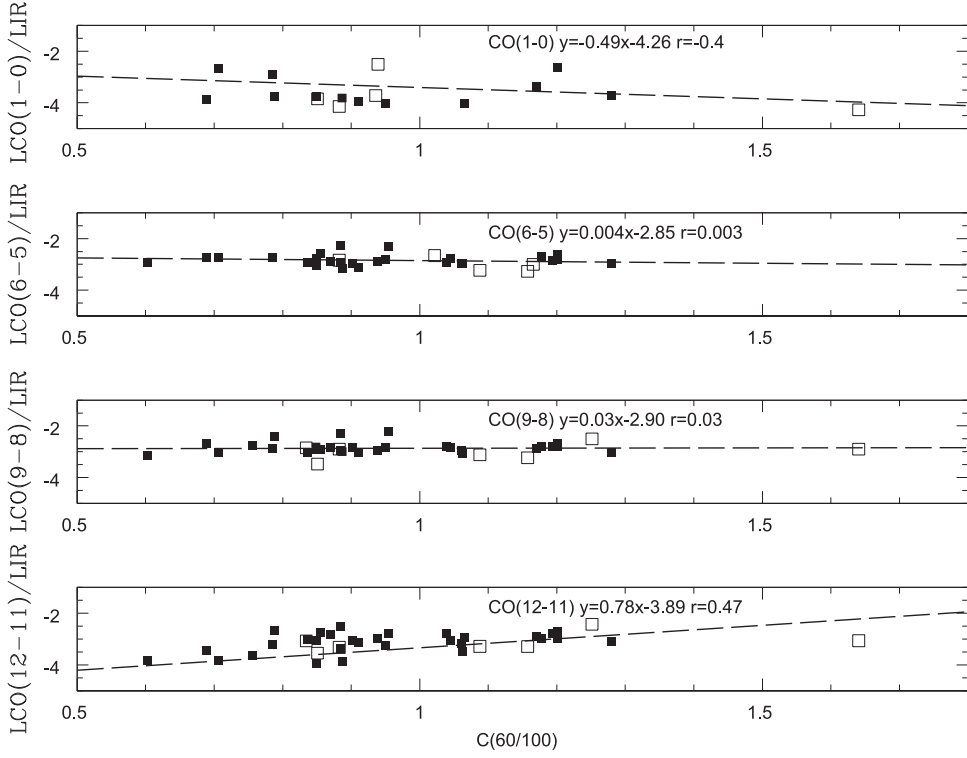


Figure 17. CO/ L_{FIR} line ratios as a function of dust temperature, parameterized as S60/S100 infrared color (open squares are sources with $S25/S60 > 0.2$). Parameters for regression analysis and the correlation coefficient are also shown. At low J values, e.g., CO(1–0), there is a poor correlation with L_{FIR} . However, between CO(6–5) and CO(9–8) the slope becomes flatter, i.e., independent of temperature with the CO(6–5) or CO(8–7) transitions. From CO($J > 11$) onward the line strength again deviate from L_{FIR} , possibly due to gas heating due to other sources such as shocks and XDRs.

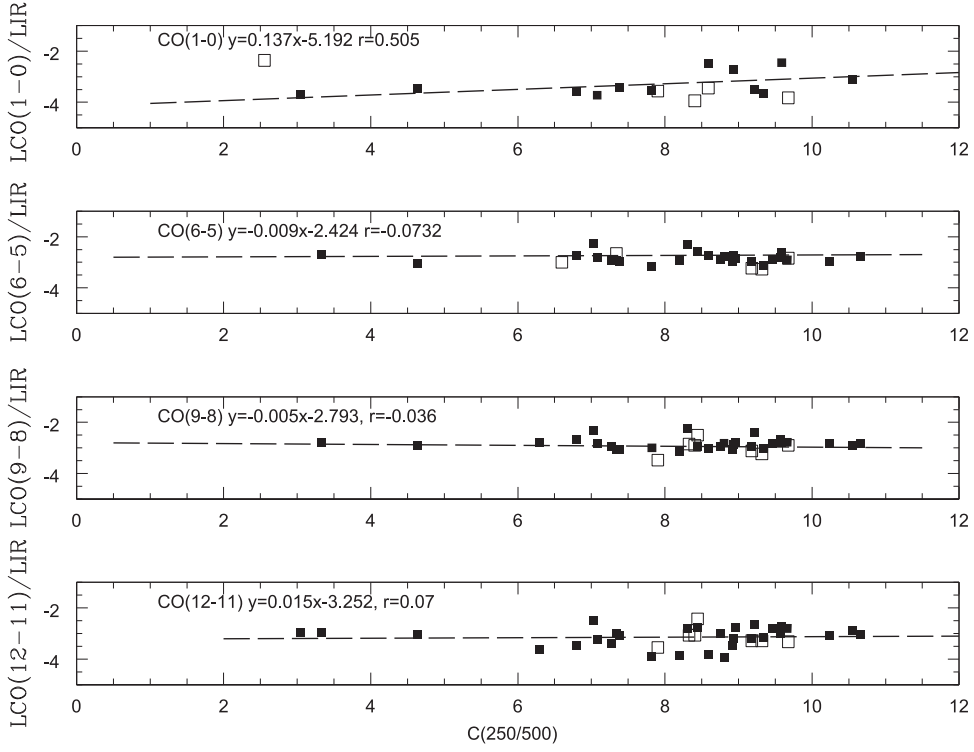


Figure 18. The CO/ L_{FIR} line ratios as a function of dust temperature, parameterized via the SPIRE S₂₅₀/S₅₀₀ color (open squares are sources with $S25/S60 > 0.2$).

S_{250}/S_{500} ratio shows a different behavior; a positive correlation with $L_{\text{CO}(1-0)}/L_{\text{IR}}$, and approximately flat relations with the other CO line ratios (Figure 17).

We checked these results by repeating the analysis for the C(60/100) indices using PACS data. The PACS indices were estimated from continua measurements around the [OI] $\lambda 63 \mu\text{m}$

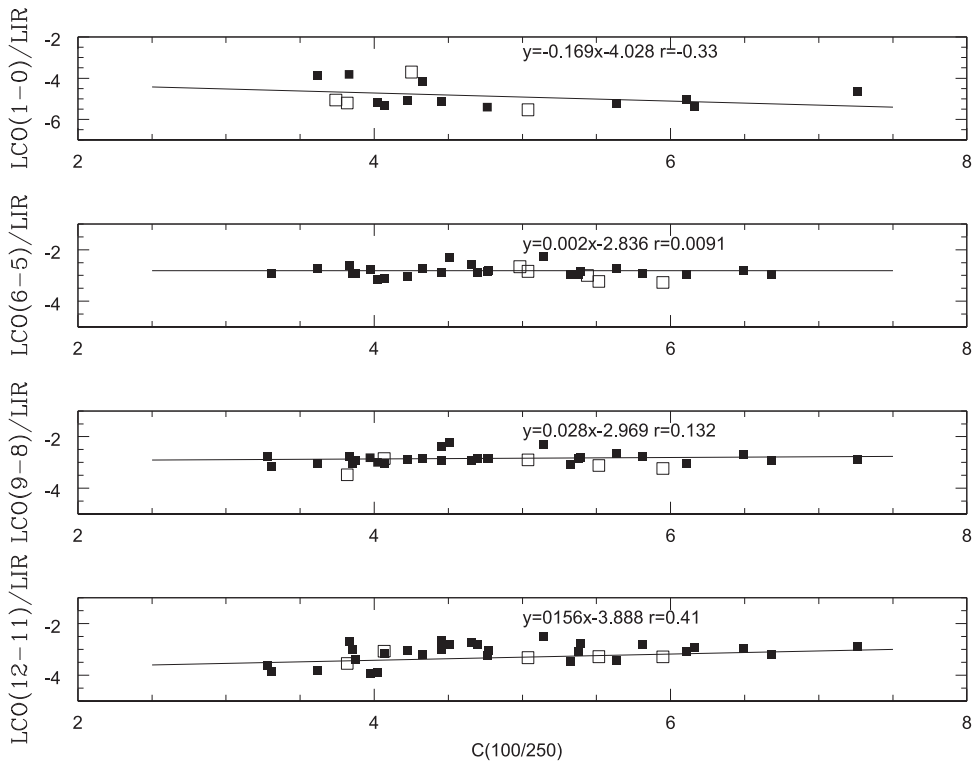


Figure 19. The CO/L_{FIR} line ratios as a function of dust temperature, parameterized via the S100/S₂₅₀ color (open squares are sources with S25/S60 > 0.2).

and [N II] λ 122 μm lines. However, the PACS observations of the HERUS ULIRGs include only a sub-sample of the SPIRE FTS sample. Nonetheless, it is reassuring that we find similar slopes for the CO(6–5), CO(9–8), and CO(12–11) correlations. The CO(1–0) data show a larger scatter, which we attribute to smaller number statistics from the smaller sample.

In what follows we outline a simple scenario that matches, at least quantitatively, these results. For starbursts in local ULIRGs, the total IR luminosity is a proxy for the total number of hot young stars in the starburst, largely independent of how those stars are distributed. The S₆₀/S₁₀₀ (and to a certain extent the S₁₀₀/S₂₅₀ ratio) ratio, on the other hand, traces the broad-scale geometry of the starburst—how compact it is given the number of stars it has—with a higher ratio implying greater compactness. This can be justified in terms of the correlation found between the equivalent width of OH(65) and C(60/100) in González-Alfonso et al. (2015).

The S₂₅₀/S₅₀₀ ratio, on the other hand, traces cold but star-formation-heated dust, whose properties are more decoupled from the CO gas reservoir than those of the hotter dust. These ratios may also provide an indication of the age and star formation history of the starburst, therefore determining the relative amounts of hot, warm, and cold gas.

Turning to the CO lines, the baseline assumption is that the CO(1–0) line is tracing the bulk of the cold CO gas reservoir, at some distance from star-forming regions. The lines from approximately CO(6–5) through CO(9–8), on the other hand, trace warmer CO in the outer parts of PDRs, or the nearby ISM. Finally, CO lines from approximately CO(12–11) and up trace hot CO in the inner PDRs or HII regions. Their luminosities are thus affected by small-scale “microphysics” of the starburst, giving rise to a larger scatter with FIR color, since this measures the geometry on larger scales of the star-forming

regions. A consequence of this scenario is that CO SLEDs of star-forming ULIRGs could be matched with three components; a cold gas component, responsible for the low- J ($J < 4$) transitions, a “warm” gas component giving rise to the mid- J transitions, and a “hot” gas component that is responsible for $J > 9$ transitions. This component will likely also have a contribution from AGN-heated gas.

This simple picture is complicated, however, by more energetic processes that are likely to be present in the majority of ULIRGs. Mechanical heating (supernova-driven turbulence, shocks) are also likely to be present and play a major role in powering CO transitions with $J > 6$ (e.g., Greve et al. 2014). The detection of water transitions in particular immediately suggests that shocks are likely to play a role. For example, although not a ULIRG, the CO SLED of NGC 1266 has been modeled with a combination of low velocity C-shocks and PDRs (Pellegrini et al. 2013).

We defer a rigorous analysis of this possibility to P.D. Hurley et al. (2016, in preparation), but here show three illustrative examples. Using RADEX we searched a large grid of temperatures (T_{kin}), densities ($n(\text{H}_2)$), column densities (N_{CO}), line widths, and source sizes, for single component fits. The parameter space is searched using the nested sampling routine MULTINEST (Ferorz & Hobson 2008), which uses Bayesian evidence to select the best model and samples multiple nodes and/or degeneracies using posterior distributions. The details of the modeling can be found in Rigopoulou et al. (2013). From these fits, we can extract maximum-likelihood contours for key physical parameters. Adopting such a process allows the effects of combining *Herschel* and ground-based CO data to be examined. Figures 20 and 21 show examples of such an extraction, for two ULIRGs, IRAS 20087-0308 and IRAS 20414-1651, respectively, for which we have

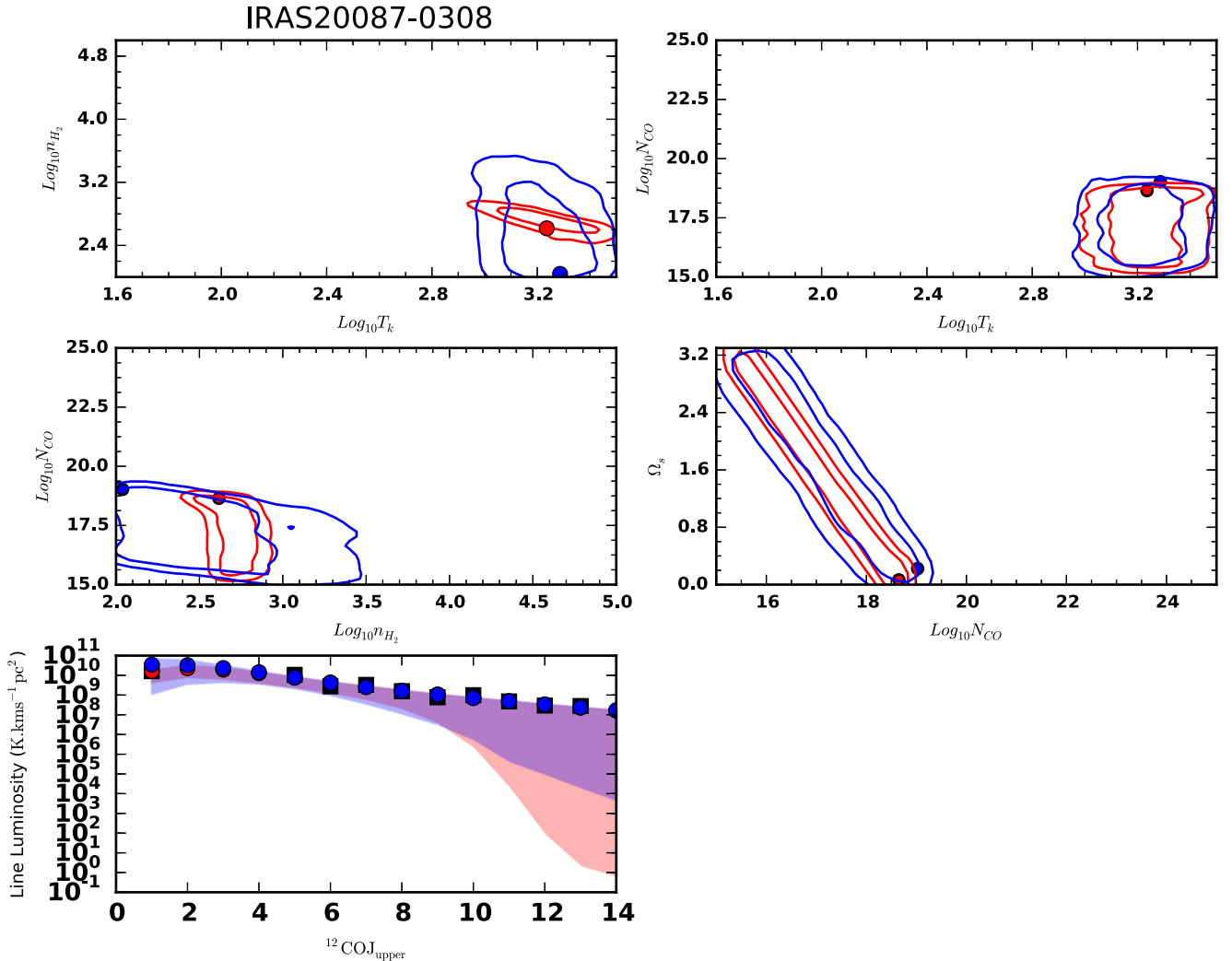


Figure 20. Example maximum-likelihood single component fit to IRAS 20087–0308. We select this object, as it shows any evidence for shock-heated gas in its optical spectra. The upper four panels show the parameter constraints achieved with only the SPIRE data (blue), and with the SPIRE and ground-based data (red). The lower panel shows the CO SLED, where the black squares are the observed data (with error bars omitted for clarity), and the blue and circles are the predicted CO fluxes using just SPIRE, and SPIRE plus ground-based data, respectively. The single component model adequately reproduces the whole SLED.

obtained ground-based data. In the case of IRAS 20087–0308, a single component model can reproduce the entire CO SLED, as has been found for a small number of systems in previous studies (Kamenetzky et al. 2014; Mashian et al. 2015; Rosenberg et al. 2015). In the case of IRAS 20414–1651, however, a single component model is clearly inadequate, as it fails to reproduce the CO(1–0) emission. Conversely, in Figure 22 we show an example of a ULIRG where three components can adequately reproduce the entire CO SLED.

7. CONCLUSIONS

A CO atlas from the HERUS program has been presented for our flux-limited ($S_{60\mu m} > 1.8$ Jy) sample of 43 local ULIRGS observed with the *Herschel* SPIRE FTS instrument, with complementary SPIRE photometry at 250, 350, and 500 μm . Post-pipeline processing was employed in order to produce high-quality spectra between 194–671 μm . Our spectra were analyzed using HIPE v11, although custom-made routines were used to correct for the effects of “Cooler burps”. Our conclusions are as follows.

(1) The CO ladder from the $J = 4$ to the $J = 13$ transitions is clearly seen in multiple detections for more than half our sample. In addition, atomic carbon (607 and 370 μm) and ionized nitrogen (205 μm) fine structure lines are detected for many sources, along with the detection of various water lines. The important ionized carbon cooling line at 197 μm was detected in our highest-redshift source IRAS 00397–1312 at $z = 0.262$, where the line is redshifted into the SPIRE FTS observational bands.

We find that ULIRG CO SLEDS do not correlate with L_{FIR} . However, a comparison of the SLEDS with their FIR colors reveals a correlation between the 60 μm /100 μm color index and the slope of the CO SLED, with ULIRGs exhibiting an increasing slope, with the J transition with warmer FIR colors, and ULIRGs exhibiting a decreasing slope with a $J (>6)$ transition with cooler FIR colors. This infers that all ULIRG SLEDS require at least three different gas components, in accordance with the trends seen when examining the variation of individual line luminosities with changes in the C(60/100) color index. Mid- J transitions originate in warm gas

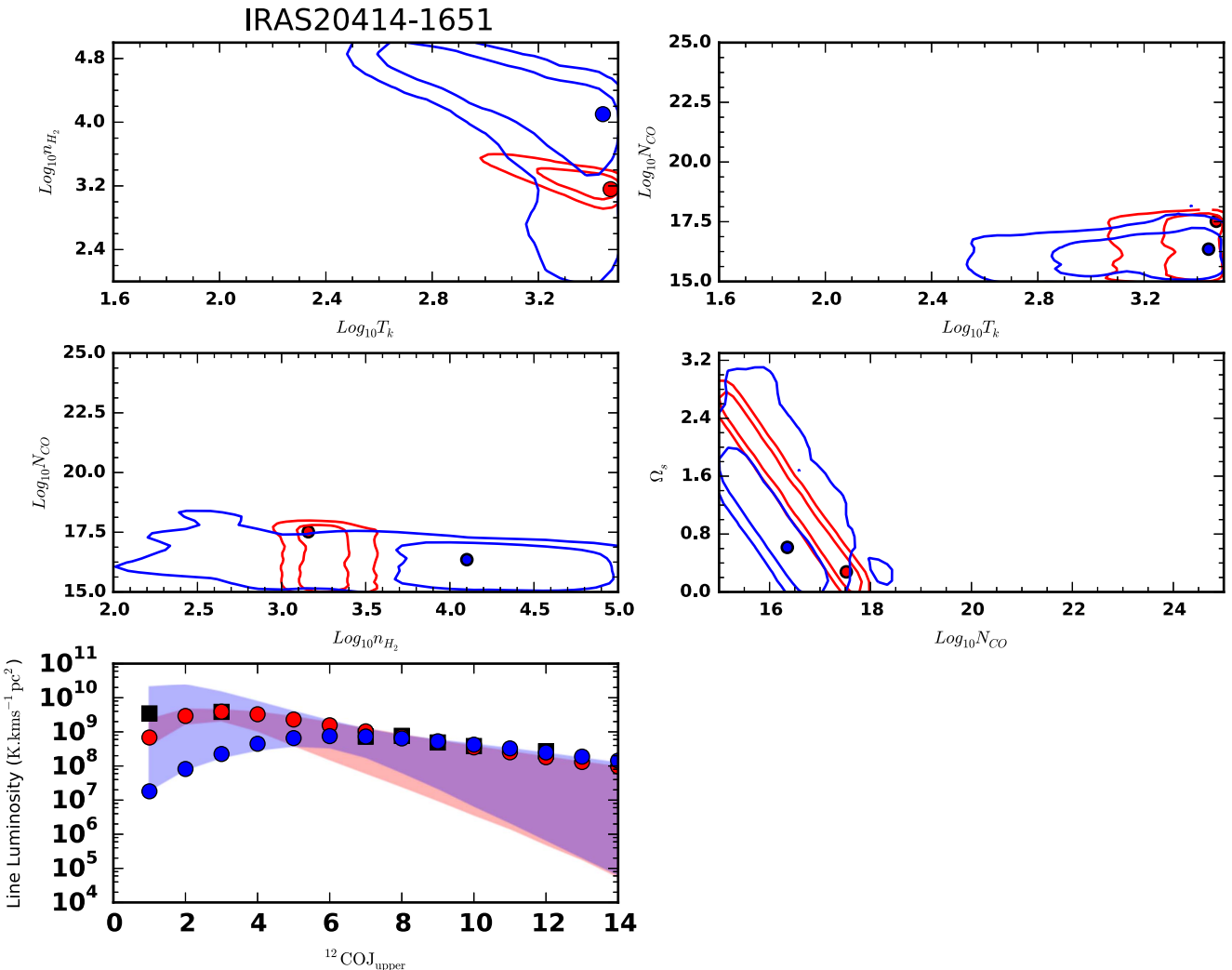


Figure 21. Example maximum-likelihood single component fit to IRAS 20414–1651. See the caption of Figure 20 for modeling details as a key to the plotted data. Here, unlike the fit to IRAS 20087–0308, a single component fit does not adequately reproduce the whole CO SLED, because it is unable to account for the lowest transition.

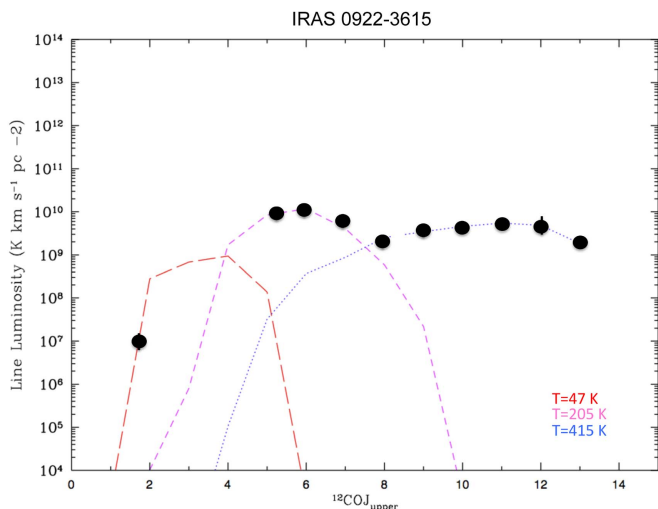


Figure 22. Example fit for a three-component temperature model generated by the Radex non-LTE radiative transfer code (van der Tak et al. 2007) for IRAS 0922–3615. The CO SLED is fit by a cold (47 K) component for the low- J transitions, a warm (205 K) component for the mid- J transitions, and a hot (415 K) component for the high- J transitions. The reduced χ^2 for this fit is below unity.

($T \sim 140$ –260 K). Since the ratio $L_{\text{mid-}J}/L_{\text{IR}}$ remains constant over a wide range of $C(60/100)$, we suggest that the gas originating in these mid- J transitions is directly linked to ongoing star formation. It is likely that the hot gas component in ULIRGs is also associated with shocks or processes directly linked to the presence of AGNs (XDRs), although we cannot probe this further based on the current data sets.

SPIRE has been developed by a consortium of institutes led by Cardiff Univ. (UK) and including: Univ. Lethbridge (Canada); NAOC (China); CEA, LAM (France); IFSI, Univ. Padua (Italy); IAC (Spain); Stockholm Observatory (Sweden); Imperial College London, RAL, UCL-MSSL, UKATC, Univ. Sussex (UK); and Caltech, JPL, NHSC, Univ. Colorado (USA). This development has been supported by national funding agencies: CSA (Canada); NAOC (China); CEA, CNES, CNRS (France); ASI (Italy); MCINN (Spain); SNSB (Sweden); STFC, UKSA (UK); and NASA (USA). HIPE is a joint development by the *Herschel* Science Ground Segment Consortium, consisting of the ESA, the NASA *Herschel* Science Center, and the HIFI, PACS and SPIRE consortia. J.A. gratefully acknowledges support from the Science and

Technology Foundation (FCT, Portugal) through the research grants PTDC/FIS-AST/2194/2012 and UID/FIS/04434/2013.

Facility: Herschel.

REFERENCES

- Armut, L., Charmandaris, V., Bernard-Salas, J., et al. 2007, *ApJ*, **656**, 148
 Béthermin, M., Daddi, E., Magdis, G., et al. 2014, arXiv:1409.5796
 Boller, T., Gallo, L. C., Lutz, D., & Sturm, E. 2002, *MNRAS*, **336**, 1143
 Cicone, C., Maiolino, R., Sturm, E., et al. 2014, *A&A*, **562**, 21
 Clements, D. L., Sutherland, W. J., Saunders, W., et al. 1996, *MNRAS*, **279**, 459
 Desai, V., Armut, L., Spoon, H. W. W., et al. 2007, *ApJ*, **669**, 810
 Dowell, C., Pohlen, M., Pearson, C. P., et al. 2010, *Proc. SPIE*, **7731**, 36
 Downes, D., Solomon, P. M., & Radford, S. J. E. 1993, *ApJL*, **414**, L13
 Efstathiou, A., Pearson, C., Farrah, D., et al. 2014, *MNRAS*, **437**, 16
 Elbaz, D., Dickinson, M., Hwang, H. S., et al. 2011, *A&A*, **533**, 119
 Farrah, D., Bernard-Salas, J., Spoon, H. W. W., et al. 2007, *ApJ*, **667**, 149
 Farrah, D., Lebouteiller, V., Spoon, H. W. W., et al. 2013, *ApJ*, **776**, 38
 Farrah, D., Lonsdale, C. J., Weedman, D. W., et al. 2008, *ApJ*, **677**, 957
 Farrah, D., Rowan-Robinson, M., Oliver, S., et al. 2001, *MNRAS*, **326**, 1333
 Ferorz, F., & Hobson, M. P. 2008, *MNRAS*, **384**, 449
 Feruglio, C., Maiolino, R., Piconcelli, E., et al. 2010, *A&A*, **518**, 155
 Fischer, J., Sturm, E., Gonzalez-Alfonso, E., et al. 2010, *A&A*, **518**, L41
 Fulton, T., Baluteau, J.-P., Bendo, G., et al. 2010, *Proc. SPIE*, **7731**, 34
 Fulton, T., Naylor, D. A., Polehampton, E. T., et al. 2016, *MNRAS*, **458**, 1977
 González-Alfonso, E., Fischer, J., Aalto, S., & Falstad, N. 2014, *A&A*, **567**, A91
 González-Alfonso, E., Fischer, J., Bruderer, S., et al. 2013, *A&A*, **550**, A25
 González-Alfonso, E., Fischer, J., Isaak, K., et al. 2010, *A&A*, **518**, L43
 González-Alfonso, E., Fischer, J., Sturm, E., et al. 2015, *ApJ*, **800**, 69
 Greve, T. R., Leonidaki, I., Xilouris, E. M., et al. 2014, *ApJ*, **794**, 142
 Griffin, M. J., Abergel, A., Abreu, A., et al. 2010, *A&A*, **518**, L3
 Hailey-Dunsheath, S., Nikola, T., Stacey, G. J., et al. 2010, *ApJL*, **714**, L162
 Hailey-Dunsheath, S., Sturm, E., Fischer, J., et al. 2012, *ApJ*, **755**, 57
 Hopwood, R., polehampton, E. T., Valtchanov, I., et al. 2015, *MNRAS*, **449**, 2274
 Houck, J. R., Roellig, T. L., Van Cleve, J., et al. 2004, *ApJS*, **154**, 18
 Kamenetzky, J., Rangwala, N., Glenn, J., Maloney, P. R., & Conley, A. 2014, *ApJ*, **795**, 174
 Kamenetzky, J., Rangwala, N., Glenn, J., Maloney, P. R., & Conley, A. 2016, *ApJ*, **829**, 93
 Kaufman, M. J., Wolfire, M. G., Hollenbach, D. J., & Luhman, M. L. 1999, *ApJ*, **527**, 795
 Kim, D. C., & Sanders, D. B. 1998, *ApJS*, **119**, 41
 Le Floc'h, E., Papovich, C., Dole, H., et al. 2005, *ApJ*, **632**, 169
 Lipari, S. 1994, *ApJ*, **436**, 102
 Lonsdale, C. J., Farrah, D., & Smith, H. E. 2006, *Astrophysics Update* 2 (Chichester: Praxis Publishing)
 Lu, N., Zhao, Y., Xu, C. K., et al. 2014, *ApJL*, **787**, L23
 Luhman, M. L., Satyapal, S., Fischer, J., et al. 1998, *ApJL*, **504**, L11
 Luhman, M. L., Satyapal, S., Fischer, J., et al. 2003, *ApJ*, **594**, 758
 Magdis, G. E., Daddi, E., Elbaz, D., et al. 2011, *ApJL*, **740**, L15
 Magdis, G., Rigopoulou, D., Hopwood, R., et al. 2014, *ApJ*, **796**, 63
 Mashian, N., Sturm, E., Sternberg, A., et al. 2015, *ApJ*, **802**, 81
 Meijerink, R., Kristensen, L. E., & Weiss, A. 2013, *ApJL*, **762**, L16
 Meijerink, R., & Spaans, M. 2005, *A&A*, **436**, 397
 Melnick, J., & Mirabel, I. F. 1990, *A&A*, **231**, L19
 Murphy, E. J., Chary, R.-R., Dickinson, M., et al. 2011, *ApJ*, **732**, 126
 Ott, S. 2010, in *ASP Conf. Ser.* 434, *Astronomical Data Analysis Software and Systems XIX*, ed. Y. Mizumoto et al. (San Francisco, CA: ASP), **139**
 Pearson, C., Lim, T., North, C., et al. 2014, *ExA*, **37**, 175
 Pellegrini, E. W., Smith, J. D., Wolfire, M. G., et al. 2013, *ApJL*, **779**, L19
 Pereira-Santaela, M., Spinoglio, L., Busquet, G., et al. 2013, *ApJ*, **768**, 55
 Pilbratt, G., Riedinger, J. R., Passvogel, T., et al. 2010, *A&A*, **518**, L1
 Poglitsch, A., Waelkens, C., Geis, N., et al. 2010, *A&A*, **518**, L2
 Pope, A., Scott, D., Dickinson, M., et al. 2006, *MNRAS*, **370**, 1185
 Rangwala, N., Maloney, P. R., Glenn, J., et al. 2011, *ApJ*, **743**, 94
 Rigopoulou, D., Hopwood, R., Magdis, G. E., et al. 2014, *ApJL*, **781**, L15
 Rigopoulou, D., Hurley, P. D., Swinyard, B. M., et al. 2013, *MNRAS*, **434**, 2051
 Rigopoulou, D., Spoon, H. W. W., Genzel, R., et al. 1999, *AJ*, **118**, 2625
 Rosenberg, M. J. F., van der Werf, P. P., Aalto, S., et al. 2015, *ApJ*, **801**, 72
 Rowan-Robinson, M., & Crawford, P. 1989, *MNRAS*, **238**, 523
 Sanders, D. B., & Mirabel, I. F. 1996, *ARA&A*, **34**, 725
 Sanders, D. B., Scoville, N. Z., & Soifer, B. T. 1991, *ApJ*, **370**, 158
 Sanders, D. B., Soifer, B. T., Elias, J. H., et al. 1988, *ApJ*, **325**, 74
 Saunders, W., Sutherland, W. J., Maddox, S. J., et al. 2000, *MNRAS*, **317**, 55
 Savage, R., & Oliver, S. 2007, *ApJ*, **661**, 1339
 Soifer, B. T., Neugebauer, G., Matthews, K., et al. 2000, *AJ*, **119**, 509
 Soifer, B. T., Sanders, D. B., Neugebauer, G., et al. 1986, *ApJL*, **303**, L41
 Solomon, P. M., Downes, D., Radford, S. J. E., & Barrett, J. W. 1997, *ApJ*, **478**, 144
 Spoon, H. W. W., Armut, L., Marshall, J. A., et al. 2009, *ApJ*, **693**, 1223
 Spoon, H. W. W., Farrah, D., Lebouteiller, V., et al. 2013, *ApJ*, **775**, 127
 Stacey, G. J., Hailey-Dunsheath, S., Ferkhoff, C., et al. 2010, *ApJ*, **724**, 957
 Sturm, E., Poglitsch, A., Contursi, A., et al. 2011, *ApJL*, **733**, L16
 Swinyard, B., Ade, P., Baluteau, J. P., et al. 2010, *A&A*, **518**, 4
 Swinyard, B., Polehampton, E., Hopwood, R., et al. 2014, *MNRAS*, **440**, 3658
 Symeonidis, M., Vaccari, M., Berta, S., et al. 2013, *MNRAS*, **431**, 2317
 van der Tak, F. F. S., Black, J. H., Schoier, F. L., Jansen, D. J., & van Dishoeck, E. F. 2007, *A&A*, **468**, 627
 van der Werf, P. P., Isaak, K. G., Meijerink, R., et al. 2010, *A&A*, **518**, L42
 Werner, M. W., Roellig, T. L., Low, F. J., et al. 2004, *ApJS*, **154**, 1
 Wolfire, M. G., Hollenbach, D., & McKee, C. F. 2010, *ApJ*, **716**, 1191
 Wu, R., Polehampton, E., Etxaluze, M., et al. 2013, *A&A*, **556**, 116